PTEP

Prog. Theor. Exp. Phys. **2012**, 01A202 (41 pages)
DOI: 10.1093/ptep/pts001

Antisymmetrized molecular dynamics and its applications to cluster phenomena

Yoshiko Kanada-En'yo[1], Masaaki Kimura[2], and Akira Ono[3]

[1]*Department of Physics, Kyoto University, Kyoto 606-8502, Japan*
[2]*Creative Research Initiative "Sousei," Hokkaido University, Sapporo 001-0021, Japan*
[3]*Department of Physics, Tohoku University, Sendai 980-8578, Japan*

Received February 9, 2012; Accepted March 22, 2012; Published August 29, 2012

Structure and reaction studies using the antisymmetrized molecular dynamics (AMD) method are reviewed. Applications of time-independent and time-dependent versions of AMD are described. In applications of time-independent AMD to nuclear structure studies, the structures of neutron-rich nuclei such as Be, C, Ne, and Mg isotopes are described, focusing on cluster aspects. The important roles of valence neutrons are discussed. The results suggest that a variety of cluster structures appear in unstable nuclei as well as in stable nuclei. Deformation and cluster phenomena in $Z \sim N$ nuclei in p- and sd-shell regions are also discussed. The applications of time-dependent AMD include various topics such as fragmentation in heavy-ion collisions as well as nuclear responses. The AMD calculations successfully describe multifragmentation, which is one of the remarkable phenomena observed in heavy-ion collisions. The approach is able to link reactions and nuclear matter properties. The studies suggest the important balance between single-particle motions and correlations to form clusters and fragments.

1. Introduction

A nucleus is a finite quantum many-body system consisting of protons and neutrons interacting via nuclear forces. Its ground state has shell structure, in which nucleons move almost independently in an averaged field (mean field) analogously to an atomic system. The shell structure and excitation modes associated with single-particle and collective motions are important facets of the nuclear system.

On the other hand, in nuclear systems, one may also find unique characteristics different from atomic systems. One important difference is that a nucleus is a self-bound system formed by attractive nuclear forces. Because of the attraction, spatial correlations between nucleons can be rather strong and, therefore, the assembling and disassembling of nucleons occur in various ways. Furthermore, the saturation property of a nuclear system, where binding energy per nucleon and central density are almost constant independently of the mass number, implies that the assembling and disassembling of nucleons can take place with a small excitation energy. As is well known, this nuclear system characteristic manifests itself as cluster structures in which a nucleus is divided into several subunits (clusters) and nucleons are confined within each cluster. The important roles of the assembling and disassembling of nucleons continue to higher excitation energies as in intermediate-energy heavy-ion collisions where a lot of clusters and fragment nuclei are produced from a hot source whose excitation energy is typically comparable to the binding energy of a nucleus.

In spite of the importance of the cluster aspect in nuclear systems, the usual mean-field approaches often fail to describe these cluster phenomena because they take into account insufficient many-body correlations, which are essential in cluster formation. The theoretical antisymmetrized molecular dynamics method (AMD) [1–9] has been proposed in studies of heavy-ion collisions. AMD describes nuclear many-body systems by antisymmetrized products of Gaussian wave packets of nucleons and incorporates quantum effects and nucleon–nucleon collisions. It has described fragment formation in heavy-ion collisions successfully. AMD has also proved to be a powerful tool for nuclear structure study. All centers of the Gaussian packets are independently treated as variational parameters in the AMD framework, and it is possible to describe various cluster structure wave functions as well as independent-particle motion in a mean field without *a priori* assumptions. Thus, AMD has been applied to investigate various phenomena in nuclear structure and reactions.

In the early days, AMD studies were limited to light systems. This is because computational cost increases rapidly in proportion to $A^{4\sim6}$ (A is the mass number) due to the non-orthogonality of single-particle wave functions. However, AMD calculations have developed remarkably toward various nuclear systems owing to the rapid progress of computational facilities. For instance, it enabled reaction studies by AMD up to Au+Au collisions ($A \sim 400$) [10], structure studies up to pf-shell nuclei ($A \sim 40$) [11], and variational calculation after the angular momentum projection that covers up to very high excitation energies [12]. Further high-performance computing will extend the subjects of AMD studies and enable more sophisticated AMD calculations.

AMD studies have revealed that cluster phenomena emerge widely in various nuclear systems. Many exotic and novel features of clustering have been discovered and the concept of clustering has been renewed and is now being extended. Today, it is well established that clustering is an essential aspect of nuclear many-body systems as well as the mean-field aspect. The coexistence of cluster and mean-field aspects brings out rich phenomena in nuclear many-body systems as functions of excitation energy and isospin degrees of freedom (Fig. 1). As the excitation energy increases, one may see transitions from mean-field to cluster structures. In deeply bound systems such as low-lying states of stable nuclei, mean-field effects are rather strong. However, even if a nucleus has a shell-model-like structure in its ground state, developed cluster structures appear in excited states near the corresponding cluster-decay threshold energy (so-called Ikeda's threshold rule [13]). Above the threshold energy, further remarkable cluster phenomena such as alpha decays, molecular resonances, and fission etc. are known. The coexistence and competition between the clustering and mean field have been studied by AMD in a unified way within a single theoretical framework. When the excitation energy increases further, nuclear systems may enter the nuclear liquid–gas phase transition region. AMD studies have confirmed the phase transition by obtaining caloric curves for equilibrium systems. The link between the phase transition and copious fragment formation in heavy-ion collisions is now clearer with the unified description from time-dependent AMD. Another important degree of freedom in nuclear systems is the isospin asymmetry, i.e., neutron (proton) excess, which is one of the major research directions in recent nuclear physics. In the neutron-rich and proton-rich domains, the saturation law of energy and density is broken. Because of the unbalanced proton–neutron ratio, we may encounter many novel cluster phenomena in isospin asymmetric systems. Indeed, such exotic clustering phenomena as cluster structures in neutron-rich Be isotopes and isospin fractionation/distillation at liquid–gas separation in fragmentation reactions have been investigated with AMD.

In this paper, we review the AMD approach and its applications to nuclear structures and reactions. In the next section, the formulation of AMD is described. Applications of the time-independent

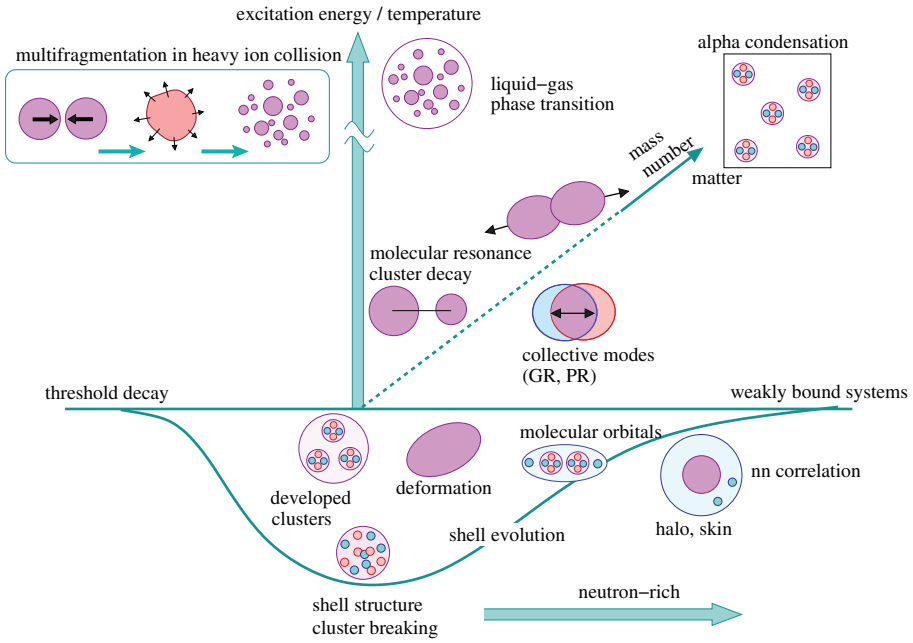

Fig. 1. Schematic figure for rich phenomena in nuclear systems.

version of AMD to static problems of nuclear structures are explained in §3, and those of the time-dependent version to dynamical phenomena such as nuclear responses and nuclear reactions are described in §4. Finally, a summary and perspectives are given in §5.

2. Antisymmetrized molecular dynamics (AMD)

As mentioned above, the cluster aspect is one of the essential features of nuclear systems as well as the mean-field aspect. Originating in the coexistence of these two kinds of nature, cluster and mean-field aspects, a variety of phenomena arise in nuclear many-body systems. To investigate the rich phenomena concerning cluster aspects such as cluster structures and multifragmentation, a theoretical framework that can describe both the cluster and mean-field features is required. The AMD method has been proved to be one of the most powerful approaches in describing these features. In this section, we briefly review the formulation of AMD. After describing the basic formalism of AMD, we explain the extended methods of AMD that have been applied to nuclear structure and nuclear reaction studies. For a detailed formulation of the AMD method, the reader is refereed to Refs. [6–9].

2.1. Basic formulation of AMD

2.1.1. AMD wave function. In the AMD framework, a basis wave function for an A-nucleon system is expressed by a Slater determinant of Gaussian wave packets:

$$\Phi_{\rm AMD}(Z) = \frac{1}{\sqrt{A!}}\mathcal{A}\{\varphi_1, \varphi_2, \ldots, \varphi_A\}, \tag{2.1}$$

where the ith single-particle wave function is written by a product of spatial (ϕ), intrinsic spin (χ), and isospin (τ) wave functions as follows.

$$\varphi_i = \phi_{\mathbf{Z}_i}\chi_i\tau_i, \tag{2.2}$$

$$\phi_{\mathbf{Z}_i}(\mathbf{r}_j) \propto \exp\left(-\nu(\mathbf{r}_j - \frac{\mathbf{Z}_i}{\sqrt{\nu}})^2\right), \tag{2.3}$$

$$\chi_i = \left(\frac{1}{2} + \xi_i\right)\chi_\uparrow + \left(\frac{1}{2} - \xi_i\right)\chi_\downarrow. \tag{2.4}$$

The spatial part $\phi_{\mathbf{Z}_i}$ of the ith single-particle wave function is represented by a complex variational parameter $Z_{i\sigma}$ with $\sigma = x, y, z$ which indicates the center of the Gaussian wave packet. The spin part χ_i is parametrized by a complex number parameter, ξ_i. The isospin function τ_i is fixed to be up (proton) or down (neutron). The width parameter ν takes a common value for all nucleons. It is chosen to be an optimum value for the studied system. Accordingly, an AMD wave function is expressed by a set of variational parameters, $Z \equiv \{\mathbf{Z}_1, \mathbf{Z}_2, \ldots, \mathbf{Z}_A, \xi_1, \xi_2, \ldots, \xi_A\}$. These parameters indicate centers of localized Gaussians and spin orientations, which are treated independently for all nucleons. That is to say, a system written by a single AMD wave function is specified by the configuration of single-nucleon wave packets in the phase space and their spin orientations. In the simplest version of AMD, the spin part χ_i is sometimes fixed to be up or down, and only parameters $\mathbf{Z}_1, \mathbf{Z}_2, \ldots, \mathbf{Z}_A$ for Gaussian centers are treated as variational parameters. In time-dependent AMD, intrinsic spin orientations are usually fixed. In the case of fixed spins, we redefine $Z \equiv \{\mathbf{Z}_1, \mathbf{Z}_2, \ldots, \mathbf{Z}_A\}$ by omitting the spin labels ξ_i.

In the AMD wave function, all single nucleons are treated independently as localized Gaussians. Although any constituent clusters are not assumed *a priori*, multi-cluster structures can be described by the grouping of single-nucleon Gaussian wave packets in the spatial configuration. On the other hand, if all the Gaussian centers gather around a certain position, the AMD wave function becomes equivalent to a harmonic oscillator shell-model wave function around the position due to the effect of antisymmetrization. Thus, the model space of AMD can describe both cluster and mean-field features with assembling and disassembling of Gaussian wave packets. If a system favors a specific cluster channel, such a cluster structure will be automatically obtained in energy variation or in dynamics.

The AMD wave function is quite similar to a wave function of fermionic molecular dynamics (FMD) [14,15] where more generalized wave functions are adopted. In applications of AMD to nuclear structure and reaction studies, the description has been improved by superposing many AMD wave functions or by introducing stochastic processes rather than by choosing more general single-particle wave functions.

2.1.2. Equation of motion. In the time-dependent versions of the AMD method which have been applied to dynamics of nuclear systems, the time evolution of the variational parameters Z are determined by the time-dependent variational principle. The equation of motion for Z derived from the time-dependent variational principle is

$$i\hbar\sum_{j\rho} C_{i\sigma,j\rho}\frac{dZ_{j\rho}}{dt} = \frac{\partial\mathcal{H}}{\partial Z^*_{i\sigma}}, \tag{2.5}$$

where σ, $\rho = x, y, z$ are the labels for the components of $\mathbf{Z}_i$ ($i = 1, 2, \ldots, A$). When the spin wave function is a variable, it may be regarded as the fourth component $Z_{i4} = \xi_i$. The expectation value of the Hamiltonian $\hat{H}$ is given by

$$\mathcal{H}(Z, Z^*) = \frac{\langle \Phi_{\rm AMD}(Z)|\hat{H}|\Phi_{\rm AMD}(Z)\rangle}{\langle \Phi_{\rm AMD}(Z)|\Phi_{\rm AMD}(Z)\rangle}. \tag{2.6}$$

A positive definite Hermitian matrix

$$C_{i\sigma,j\rho} \equiv \frac{\partial^2}{\partial Z^*_{i\sigma}\partial Z_{j\rho}} \ln\langle \Phi_{\rm AMD}(Z)|\Phi_{\rm AMD}(Z)\rangle \tag{2.7}$$

appears in the equation of motion, suggesting that the variables Z are not canonical coordinates.

2.1.3. Energy variation. To get an optimum solution for the energy minimum state, the energy variation is performed. Namely, the variational parameters Z are optimized to minimize the expectation value of the Hamiltonian in the AMD model space. We introduce the following frictional cooling equation:

$$i\hbar \sum_{j\rho} C_{i\sigma,j\rho} \frac{dZ_{j\rho}}{dt} = (\lambda + i\mu) \frac{\partial \mathcal{H}}{\partial Z^*_{i\sigma}}. \tag{2.8}$$

The parameter λ is an arbitrary real number and μ is an arbitrary negative real number. It is easily proved that the energy of the system decreases as time develops due to the frictional term $i\mu$. In the energy variation, the matrix $C_{i\sigma,j\rho}$ can be replaced with $\delta_{ij}\delta_{\sigma\rho}$ and then the frictional cooling method with $\lambda = 0$ becomes equivalent to the steepest descent method. In both cases of $C_{i\sigma,j\rho}$, we obtain the optimum set of parameters Z that gives the AMD wave function for the minimum energy state in the model space after enough cooling time (iteration steps).

2.1.4. Hamiltonian. The Hamiltonian for an A-nucleon system consists of the kinetic energy and the nuclear and Coulomb force terms:

$$\hat{H} = \sum_i \hat{t}_i + \sum_{i,j} \hat{v}_{ij} + \sum_{i,j} \hat{v}^{\rm coulomb}_{ij} - \hat{T}_g. \tag{2.9}$$

Here $\hat{t}_i$ is the kinetic energy. The energy of the center-of-mass motion $\hat{T}_g$ is subtracted exactly because the total wave function can be separated into the internal wave function and the center-of-mass wave function. In applications to heavy-ion collisions, spurious kinetic energy of the zero-point oscillation of fragment mass centers is also subtracted from the Hamiltonian. For the effective two-body nuclear force $\hat{v}_{ij}$, finite-range forces such as Volkov [16] forces supplemented by G3RS form spin–orbit forces [17,18], Gogny [19,20] forces, and Skyrme [21,22] forces are used. Finite-range two-body forces with zero-range three-body forces such as the modified Volkov forces [23] are also used. The Coulomb force $\hat{v}^{\rm coulomb}_{ij}$ is approximated by a sum of seven Gaussians.

These effective forces are phenomenological ones constructed to describe the low-energy properties of nuclear structure. In heavy-ion reactions, residual interactions contribute to nucleon–nucleon collisions that are incorporated by a stochastic collision process in the AMD framework as explained later.

2.2. Basis AMD and its extensions in applications

In the early stages of AMD studies, simple versions of the AMD method were applied to reaction and structure studies [1–5] and, later, the AMD method was developed to many extended versions

(Refs. [6,8,9] and references therein). In this section, we explain the formulation of the basic AMD method and some advanced versions for structure study and reaction study.

A basis AMD wave function is given by a single Slater determinant. Generally, many-body wave functions for quantum systems should be expressed by a superposition of many Slater determinants. Restriction of the model space within a single Slater determinant is the limit of a mean-field approximation. To incorporate beyond-mean-field effects, superposition of Slater determinants is essential. Firstly, in structure study, parity and angular-momentum projections, which are done by superposition of Slater determinants, are essential to describe the properties of energy-eigen states. Secondly, superposition of Slater determinants is significant to the improvement of wave functions by taking into account quantum fluctuation around a mean-field, many-body correlations, and spin-parity projections. It is also necessary to describe excited states orthogonal to lower states.

In applications of the AMD method to structure study, the projections and superposition of AMD wave functions are practically performed. In applications to heavy-ion reactions, however, the emergence of multiple reaction channels is introduced by stochastic branching processes, neglecting quantum interference between different channels, each of which is described by an AMD wave function.

2.2.1. Projections and superposition of AMD wave functions. The parity-projected AMD wave function is given as

$$|\Phi^{\pm}_{\rm AMD}\rangle \equiv P^{\pm}|\Phi_{\rm AMD}(Z)\rangle = \frac{1 \pm \hat{P}_r}{2}|\Phi_{\rm AMD}(Z)\rangle, \tag{2.10}$$

where $P^{\pm} = 1 \pm \hat{P}_r$ is the parity projection operator. The angular-momentum projected AMD wave function is written as

$$|\Phi^{J}_{MK}\rangle = P^{J}_{MK}|\Phi_{\rm AMD}(Z)\rangle = \int d\Omega D^{J*}_{MK}(\Omega)\hat{R}(\Omega)|\Phi_{\rm AMD}(Z)\rangle. \tag{2.11}$$

Here $D^{J}_{MK}(\Omega)$ is Wigner's D function and $\hat{R}(\Omega)$ is a rotation operator with respect to the Euler angle Ω. As is clearly shown, the angular-momentum projected state is expressed by a linear combination of wave functions rotated from the intrinsic AMD wave function $\Phi_{\rm AMD}(Z)$ with the weight function D^{J*}_{MK}. The matrix element of a tensor operator $\hat{T}^{k}_{q}$, where k is the rank and q is the z-component, can be calculated to be

$$\begin{aligned}\langle P^{J}_{MK}\Phi_{\rm AMD}(Z)|\hat{T}^{k}_{q}|P^{J'}_{M'K'}\Phi_{\rm AMD}(Z')\rangle &= \frac{8\pi^2}{2J+1}\langle J'M'kq|JM\rangle \\ &\times \sum_{\mu\nu}\langle J'\mu k\nu|JK\rangle \int d\Omega D^{J'*}_{\mu K'}(\Omega)\langle\Phi_{\rm AMD}(Z)|\hat{T}^{k}_{\nu}\hat{R}(\Omega)|\Phi_{\rm AMD}(Z')\rangle.\end{aligned} \tag{2.12}$$

In practical calculations, the integrations with respect to Ω are performed by numerical integration on grid points of angles $\Omega = (\theta_1, \theta_2, \theta_3)$. In calculations of expectation values for observable operators such as Hamiltonian, radii, moments, and transitions, AMD wave functions are projected to parity and angular-momentum eigenstates. In the usual AMD calculations for structure study, the parity projection is done before energy variation while the angular-momentum projection is performed after the energy variation, i.e., variation before projection (VBP).

Superposition of independent AMD wave functions is useful to improve wave functions and it is essential in the description of excited states to satisfy orthogonality between energy levels. Let us consider the superposition of the independent AMD wave functions $\Phi_{\rm AMD}(Z^{(k)})$

($k = 1, \ldots, k_{\max}$) ($k_{\max}$ is the number of adopted basis AMD wave functions). The superposed wave functions for $J^{\pm}$ states are written as

$$|\Phi_n^{J\pm}\rangle = \sum_{kK} c_{n,kJK} |P_{MK}^{J\pm} \Phi_{\rm AMD}(Z^{(k)})\rangle, \tag{2.13}$$

where $P_{MK}^{J\pm} \equiv P_{MK}^{J} P^{\pm}$. Here the values for the coefficients $c_{n,kJK}$ are determined by the variational principle,

$$\delta\{\langle\Phi_n^{J\pm}|\hat{H}|\Phi_n^{J\pm}\rangle - \epsilon_n \langle\Phi_n^{J\pm}|\Phi_n^{J\pm}\rangle\} = 0, \tag{2.14}$$

which is equivalent to diagonalization of the norm and the Hamiltonian matrices and leads to the Hill–Wheeler equations. The K sum in Eq. (2.13) stands for K-mixing.

To adopt efficient AMD wave functions as basis wave functions for the superposition, constraint methods, which are often used in a generator coordinates method (GCM) [24–27], or stochastic variational methods [28] are applied in the AMD framework. Here we consider a constraint $\langle\hat{g}\rangle = \bar{g}$. By changing the constraint value as $\bar{g} = \bar{g}_1, \bar{g}_2, \ldots, \bar{g}_{k_{\max}}$, the minimum energy state $\Phi_{\rm AMD}^{\pm}(\bar{g})$ in the AMD model space is obtained for each constraint value by the constraint energy variation after parity projection. Then the obtained wave functions $\Phi_{\rm AMD}^{\pm}(\bar{g}_k)$ ($k = 1, \ldots, k_{\max}$) are superposed, and coefficients are determined by the diagonalization. This method corresponds to a GCM calculation for a generator coordinate $\bar{g}$ when a sufficient number of basis wave functions for different values $\bar{g}_k$ are taken into account. This method (called AMD + GCM) is useful, in particular, for the study of excited states. For the constraints, nuclear quadrupole deformation parameters are often used [25–27]. In the AMD + GCM method, variation is done before the angular-momentum projection.

It is also efficient to perform variation after the angular-momentum projection as well as the parity projection, especially for the study of excited states. Namely, the energy expectation value for a parity and angular-momentum projected AMD wave function,

$$\mathcal{H} = \frac{\langle P_{MK}^{J\pm}\Phi_{\rm AMD}(Z)|\hat{H}|P_{MK}^{J\pm}\Phi_{\rm AMD}(Z)\rangle}{\langle P_{MK}^{J\pm}\Phi_{\rm AMD}(Z)|P_{MK}^{J\pm}\Phi_{\rm AMD}(Z)\rangle}, \tag{2.15}$$

is minimized with respect to the variational parameters Z by using the frictional cooling method. Firstly, for a given spin and a parity $J^{\pm}$, the wave function for the lowest $J^{\pm}$ state is obtained by the energy variation. Then, a wave function for a higher state ($J_n^{\pm}$) is provided by varying Z to minimize the energy for the component of an AMD wave function orthogonal to the lower states ($J_1^{\pm}, \ldots, J_{n-1}^{\pm}$) which are already obtained. In the present paper, we call the variation after spin-parity projection "VAP" [12].

2.2.2. Extensions for single-particle wave functions. In a basis AMD wave function, a single-particle wave function is written by a spherical Gaussian. In extended versions of AMD, a single-particle wave function is written by a deformed Gaussian or superposition of different-range Gaussians to improve single-particle wave functions [25,26,29,30]. In the method of deformed-basis AMD [25,26], triaxially deformed Gaussians are employed as single-particle wave packets instead of spherical ones,

$$\phi_{\mathbf{Z}_i}(\mathbf{r}_j) \propto \exp\left\{-\sum_{\sigma=x,y,z} \nu_\sigma \left(r_{j\sigma} - \frac{Z_{i\sigma}}{\sqrt{\nu_\sigma}}\right)^2\right\}, \tag{2.16}$$

where the width parameters, ν_x, ν_y and ν_z, take different values for each direction. They are determined in the energy variation to optimize the energy of a system. By using this deformed basis, it

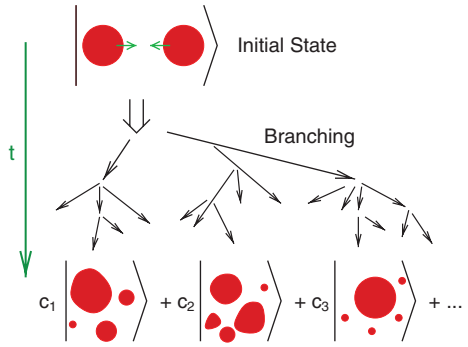

Fig. 2. A schematic picture of the quantum branching processes for multichannel reactions.

is possible to successfully describe the coexistence (or mixing) of cluster and deformed mean-field structures, which are essential especially in heavy systems.

Superposing different range Gaussians is another method of improving the single-particle wave functions of an AMD wave function, as is done in the FMD method [29,30].

Instead of adopting deformed or superposing Gaussians, a method of stochastic branching on wave packets is used to describe the diffusion and deformation of single-particle motions in the time-dependent version of AMD for nuclear reaction calculations [10,31,32], as explained in the next subsection.

2.3. Branching in time evolution

The description of dynamics of excited nuclear many-body systems, such as in heavy-ion collisions, is a highly quantum-mechanical many-body problem. If the many-body time-dependent Schrödinger equation is solved for an initial state which may be roughly approximated by a single Slater determinant, the intermediate and final states will be very complicated states containing a huge number of reaction channels corresponding to different fragmentation configurations, as illustrated in Fig. 2. The AMD model for reactions respects the existence of channels, while it neglects some of the interference among them. Namely, the total many-body wave function $|\Psi(t)\rangle$ is approximated by a mixed state

$$|\Psi(t)\rangle\langle\Psi(t)| \approx \int \frac{|\Phi(Z)\rangle\langle\Phi(Z)|}{\langle\Phi(Z)|\Phi(Z)\rangle} w(Z,t)dZ, \tag{2.17}$$

where each component is represented by an AMD wave function $|\Phi(Z)\rangle$ with a time-dependent weight $w(Z,t)$.

Interference between quite different components is not of practical importance because the matrix elements are negligible for the Hamiltonian and other operators of interest. Furthermore, when we adopt the mean-field approximation in some way, we need to take care of the spurious nonlinearity introduced by the approximation. A many-body state composed of different reaction channels cannot be described by a single mean field. Our strategy is to suitably decompose the state in such a way that the mean-field approximation is valid in each component.

Let us consider the motion of a nucleon in the system, ignoring the Pauli principle for the moment. In the mean-field approximation, the one-body density matrix is given by a pure single-particle wave function $\hat{\rho}(t) = |\psi(t)\rangle\langle\psi(t)|$ at any time. Under the mean field, the phase space distribution will spread in some directions and may shrink in other directions. In contrast, in real time evolution,

the condition $\hat{\rho}(t)^2 = \hat{\rho}(t)$ should no longer hold due to many-body correlations. Namely, decoherence should occur on the single-particle state so that it turns into a mixed state. In the AMD approach, decoherence is taken into account by splitting the wave packet in such a way that the spreading of the distribution in the mean field is respected while shrinking is discarded. By the decoherence of the single-particle states, the decomposition (or branching) of the many-body state is induced naturally. This approach of using compact wave packets is advantageous for the case with many fragmentation channels because it is free from spurious coupling of different fragmentation channels.

Instead of directly considering the weight function $w(Z, t)$ in Eq. (2.17), we solve a stochastic equation of motion for the wave packet centroids Z, which may be symbolically written as

$$\frac{d}{dt}\mathbf{Z}_i = \{\mathbf{Z}_i, \mathcal{H}\}_{\rm PB} + (\text{NN coll}) + \Delta\mathbf{Z}_i(t) + \mu(\mathbf{Z}_i, \mathcal{H}'). \tag{2.18}$$

The first term $\{\mathbf{Z}_i, \mathcal{H}\}_{\rm PB}$ is that in the deterministic equation of motion [Eq. (2.5)] derived from the time-dependent variational principle.

The second term represents the effect of stochastic two-nucleon collisions, where a parametrization of the energy-dependent in-medium cross section is adopted. The collisions are performed with the "physical nucleon coordinates" that take account of the antisymmetrization effects, and then the Pauli blocking in the final state is automatically introduced [1,2].

The third term $\Delta\mathbf{Z}_i(t)$ is a stochastic term for the wave packet splitting mentioned above [10,31,32]. The change of the width and shape of each wave packet is calculated by solving the Vlasov equation (for some time period) with the same effective interaction as for the term $\{\mathbf{Z}_i, \mathcal{H}\}_{\rm PB}$. An essential ingredient here is how long the coherent single-particle motion is solved before decoherence. The properties of fluctuations $\Delta\mathbf{Z}_i(t)$ are determined depending on this time scale, called the coherence time τ. When wave packet splitting was first introduced into AMD [10,31], the limit of $\tau \to 0$ was taken, for which the decoherence effect is maximum. The choice of a finite coherence time has been formulated in Ref. [32], and a reasonable choice may be to consider decoherence for a nucleon when it collides with another nucleon. This choice is symbolically denoted by $\tau = \tau_{\rm NN}$, though τ is not a constant number.

The last term $\mu(\mathbf{Z}_i, \mathcal{H}')$ is a dissipation term related to the fluctuation term $\Delta\mathbf{Z}_i(t)$. This term is necessary in order to restore the energy conservation that is violated by the fluctuation term. The coefficient μ is given by the condition of energy conservation. However, the form of this term is somehow arbitrary. The variables Z are shifted to the direction of the gradient of the energy expectation value $\mathcal{H}$ under the constraints of nine conserved quantities (the center-of-mass variables and the total angular momentum). When the number of other nucleons around the nucleon i within a phase space radius of $|\mathbf{Z}_j - \mathbf{Z}_i| < 2.5$ is more than a certain number $N_{\rm c9}$, another twelve global one-body quantities (monopole and quadrupole moments in coordinate and momentum spaces) are also included as constrained quantities for the dissipation corresponding to the fluctuation $\Delta\mathbf{Z}_i(t)$. The latter constraints should be imposed because the one-body time evolution has already been considered by $\{\mathbf{Z}_i, \mathcal{H}\}_{\rm PB} + \Delta\mathbf{Z}_i(t)$. Empirically, $N_{\rm c9}$ has been chosen between 5 and 15.

A summary of the complete formulation of AMD for reactions can be found in Ref. [6].

3. Applications of the time-independent AMD method to nuclear structure

Here we discuss some topics investigated with the time-independent AMD method, focusing on cluster aspects.

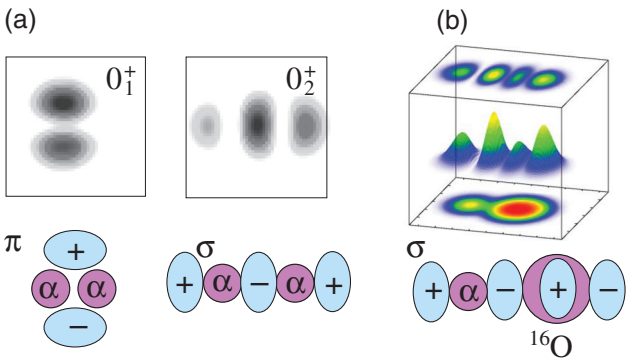

Fig. 3. (a) Density distributions of the single-particle wave functions for valence neutrons in ^{10}Be(0_1^+) and ^{10}Be(0_2^+) [54]. Schematic figure of the molecular orbitals; π and σ orbitals around the 2α core are also shown at the bottom. (b) Density distribution of the excited band ($K^\pi = 0^-$) in ^{22}Ne obtained by AMD [46]. The middle and top figures show the density distribution of the single-neutron wave function of the highest single-particle level. The matter density of the total system is displayed at the bottom of the box.

3.1. Molecular structures in Be and Ne isotopes

The cluster structure of Be isotopes is one of the most fascinating subjects of unstable nuclei. A 2α-cluster core is favored in neutron-rich Be isotopes as well as ^{8}Be whose ground state is a 2α resonance state. The low-lying states of neutron-rich Be isotopes are described well by a molecular-orbital picture based on a 2α core and valence neutrons moving around the 2α [33–42]. In contrast to the molecular-orbital structures in low-lying states, developed di-cluster states such as ^{6}He + ^{6}He in ^{12}Be have been suggested in highly excited states [9,41,43–45]. There, valence neutrons move not around the whole system but around one of two α clusters. This means that a variety of cluster structures coexist in neutron-rich Be isotopes where valence neutrons play important roles.

The molecular-orbital picture has also been extended to Ne isotopes such as ^{21}Ne and ^{22}Ne based on an ^{16}O+α-cluster core and valence neutrons in molecular orbitals [9,36,37,46]. Di-cluster states like ^{18}O+α-cluster states in ^{22}Ne are another attractive subject [9].

3.1.1. Molecular-orbital structure. The idea of the molecular orbitals surrounding a 2α core was suggested in ^{9}Be with a 2α + n cluster model[47–49] in the 1970s. In the 1980s and 1990s, molecular-orbital models were applied to neutron-rich Be isotopes and succeeded in describing rotational bands [33–39].

In a 2α system, molecular orbitals are formed by a linear combination of p orbits around two α clusters. In neutron-rich Be isotopes, valence neutrons occupy the molecular orbitals around the 2α core. The negative-parity orbital is called the "π orbital", while the longitudinal orbital with positive parity is the "σ orbital" (Fig. 3). Since the σ orbital has two nodes along the α–α direction, it gains kinetic energy as the 2α cluster develops. The energy gain of the σ orbital in the developed 2α system results in the intruder configurations of the ^{11}Be and ^{12}Be ground states. In other words, it is the origin of the breaking of the neutron magic number $N = 8$ in Be isotopes.

In analogy to neutron-rich Be isotopes, molecular-orbital structures in Ne isotopes have been suggested from experimental systematics [36,37]. Indeed, AMD calculation has predicted the presence of molecular-orbital bands with an ^{16}O+α-cluster core surrounded by two valence neutrons in the σ orbital [9,46]. Unlike Be isotopes, the σ orbital is a linear combination of sd orbits around ^{16}O and p orbits around α, and it results in a pf-shell-like molecular orbital. Another difference is the parity asymmetry of the core, which produces the parity doublet of the molecular bands. Similar

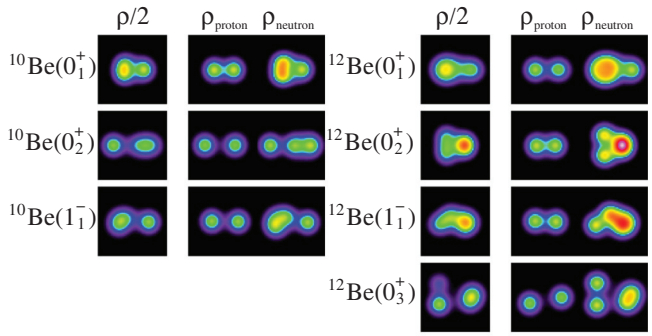

Fig. 4. Density distributions of the intrinsic states for the band-head states of ^{10}Be and ^{12}Be obtained by AMD-VAP [44,54]. The integrated densities of matter, proton, and neutron densities are presented in the left, middle, and right panels.

molecular-orbital structures have been also suggested for F isotopes [50]. Detailed discussions are given in later sections.

3.1.2. Cluster structures in neutron-rich Be isotopes. Cluster structures of Be isotopes have been intensively investigated in many theoretical works with cluster models [45,51–53], molecular-orbital models [33–35,38,39,42,47–49], and AMD [8,40,44,54,55]. In the cluster and molecular-orbital models, the existence of two α clusters are *a priori* assumed. On the other hand, AMD does not rely on model assumptions of the existence of cluster cores. Nevertheless, the results of AMD calculations indeed indicate the appearance of the 2α core surrounded by valence neutrons in the molecular orbitals in low-lying states of Be isotopes. This means that the formation of the 2α core and molecular orbitals has been theoretically confirmed by those AMD calculations without assuming clusters. Here we discuss the cluster structures of neutron-rich Be isotopes based on AMD calculations [8,44,54,55].

A systematic study of the ground and excited states of Be isotopes was performed with VAP calculations in the AMD model (AMD-VAP). Many rotational bands with a 2α core structure were obtained in the theoretical results. In Fig. 4, density distributions of the intrinsic wave functions for the band-head states of ^{10}Be and ^{12}Be are shown. As is seen, the proton-density distribution indicates the formation of the 2α core, while the neutron density distribution exhibits the behavior of valence neutrons around the 2α core.

In analysis of single-particle wave functions in the AMD wave functions, valence neutron orbits in low-lying states of Be isotopes were found to be associated with the molecular orbitals around the 2α core. In Fig. 5, we show schematic figures of the cluster states suggested in ^{10}Be, ^{11}Be, and ^{12}Be. In the figure, we show the number of neutrons occupying the σ-like orbitals, which have dominant positive-parity components and are regarded as the σ orbital. The experimental value for the excitation energies of the corresponding states are also shown in the figure.

In ^{10}Be, the valence neutron configurations of ^{10}Be(0^+_1), ^{10}Be(1^-), and ^{10}Be(0^+_2) can be regarded as π^2, $\pi\sigma$, and σ^2 configurations meaning two neutrons in the π orbitals, one neutron in the π and the other neutron in the σ, and two neutrons in the σ, respectively. Spatial distributions of the single-particle orbits of valence neutrons in ^{10}Be(0^+_1) and ^{10}Be(0^+_2) are shown in Fig. 3(a), where the π-like orbital and the σ-like orbital are clearly seen. Similarly to ^{10}Be, it was found that the ^{11}Be($1/2^+$),^{11}Be($1/2^-$), and ^{11}Be($3/2^-_2$) states correspond to $\pi^2\sigma$, π^3, and $\pi\sigma^2$ configurations, while the ^{12}Be(0^+_1), ^{12}Be(0^+_2), and ^{12}Be(1^-_1) states are roughly interpreted as $\pi^2\sigma^2$, π^4, and $\pi^3\sigma^1$ configurations.

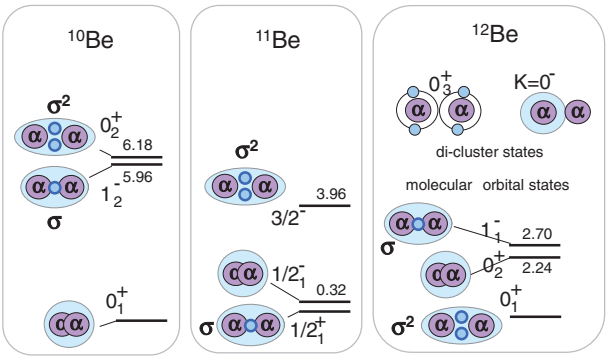

Fig. 5. Schematic figures for cluster states suggested in ^{10}Be, ^{11}Be, and ^{12}Be. For the molecular-orbital states, 2α cores and the valence neutrons in the σ orbital are illustrated. The experimental values of the excitation energies are also shown.

Interestingly, the degree of the 2α-cluster development strongly correlates with the number of valence neutrons in the σ orbital. Namely, the 2α cluster develops as the neutron number in the σ orbital increases. This is easily understood because the single-particle energy of the σ orbital decreases because of the kinetic energy gain in largely distant 2α systems. The enhancement of the 2α cluster with neutrons in the σ orbital is consistent with the arguments in Refs. [34–39]. On the other hand, as the neutron number in the π orbitals increases, the cluster structure tends to weaken.

Another interesting characteristic of Be isotopes is the breaking of neutron magicity in ^{11}Be and ^{12}Be. The breaking of the p shell for the neutron magic number $N = 8$ in ^{11}Be is experimentally known from the unnatural parity $1/2^+$ ground state, while that in ^{12}Be has been suggested from slow β decay[56]. These exotic features of ^{11}Be and ^{12}Be can be understood from the molecular-orbital picture. The ground states of ^{11}Be and ^{12}Be are considered to have dominant intruder configurations with σ-orbital neutron(s) instead of normal $0\hbar\omega$ configurations. The ground $1/2^+$ state of ^{11}Be corresponds to the $\pi^2\sigma$ configuration, while ^{12}Be(0^+_1) is the intruder state $\pi^2\sigma^2$ in terms of molecular orbitals. In the one-center shell-model limit, the π and σ orbitals correspond to the p and sd orbits. Therefore, in the ground states, ^{11}Be$(1/2^+_1)$ and ^{12}Be(0^+_1) have dominant $1\hbar\omega$ and $2\hbar\omega$ configurations, respectively, indicating the vanishing of the $N = 8$ magic number in ^{11}Be and ^{12}Be. The breaking of the neutron shell in neutron-rich Be isotopes is caused by the decreasing σ orbital in the developed 2α structures as discussed in Refs. [8,44,55]. Again, the σ orbital in the 2α structure plays an important role.

In addition to molecular-orbital structures in such low-lying states, the AMD results for ^{12}Be suggest molecular resonant states with di-cluster ^{6}He $+^6$ He and ^{8}He $+ \alpha$ structures in highly excited states [44]. This result is consistent with the experimental observations of cluster states in He + He break-up reactions [57–59] and also with theoretical suggestions by cluster model calculations [43,45,60].

3.2. Three-body cluster states in ^{12}C, ^{11}B, and ^{14}C

One of the typical examples where cluster and shell features coexist is ^{12}C. The ground state of ^{12}C is an admixture of 3α-cluster and $p_{3/2}$-shell closure structures. On the other hand, a variety of 3α-cluster states have been suggested in excited states in many 3α model calculations since the 1970s [61]. Recently, Tohsaki *et al.* have proposed a new concept of cluster structure in the second 0^+ state of ^{12}C, where three α clusters are weakly interacting like a gas [62,63]. Because of the bosonic

behavior of α particles in a dilute 3α gas state this phenomenon has been discussed in relation to Bose–Einstein condensation of α particles in dilute nuclear matter [64]. Searching for such dilute cluster gas-like states in other nuclei, for instance, ^{11}B and ^{13}C, is a challenging issue. Another interesting problem to be solved is a linear-chain 3α structure [65,66]. It has been a long-standing problem whether a linear-chain 3α state appears in excited states of ^{12}C or not. The possibility of linear-chain structures in neutron-rich C isotopes is also attracting a great deal of interest as they might be stabilized by valence neutrons.

Applying the AMD method to ^{12}C, ^{11}B, and ^{14}C, we have found various three-body cluster structures in their excited states as well as shell-model structures in low-lying states. Some are weakly interacting three-cluster states, and some shows rather geometric configurations of clusters. Here we discuss the cluster aspects of these nuclei based on AMD-VAP calculations for ^{12}C and ^{11}B [12,67,68] and β–γ constraint AMD calculations for ^{14}C [69].

3.2.1. Cluster structures of ^{12}C. To investigate the excited states of ^{12}C we performed AMD-VAP calculations. As already mentioned, in the AMD model, all nucleons are independently treated without assuming the existence of any clusters. The formation or breaking of shell structure and clusters is expressed in the twelve-nucleon dynamics after the energy variation. Even though any clusters are not *a priori* assumed, α clusters are formed in many excited states of ^{12}C. Indeed, a variety of 3α cluster states were obtained in the AMD results. The experimental and calculated energy levels of ^{12}C are shown in Fig. 6, and the density distribution of intrinsic wave functions for the ground and excited states is shown in the upper row of Fig. 7. It should be stressed that this is the first calculation that succeeded in simultaneously reproducing the energy spectra of the ground band and those of excited states having developed 3α cluster structures in ^{12}C. This success results from the flexibility of the AMD wave functions, which can describe both shell-model and cluster structures. The calculation also reproduces well transition properties such as $E2$, monopole, and GT transitions. In the result, the ground state shows the $p_{3/2}$-shell closure configuration with mixing of the 3α-core component, while the second 0^+ state has a well developed 3α cluster structure. Since the 0^+_2 wave function has a large overlap with various 3α configurations (the amplitudes of the superposed wave functions do not concentrate on a specific AMD wave function but fragment largely into various AMD wave functions), this state is regarded as the 3α gas-like state, where three α clusters are moving rather freely in a dilute density. The 3α chain-like state was suggested in the third 0^+ state around 10 MeV in the AMD result. It is not a "linear" chain but shows an obtuse triangle 3α configuration as seen in the figure. These results are quite similar to those calculated with FMD with the unitary correlation operator method (UCOM) [70].

3.2.2. Cluster structures of ^{11}B. We applied the same method, AMD-VAP, to ^{11}B and its mirror nucleus ^{11}C, and investigated the structures while focusing on the cluster aspect. The energy levels of the negative-parity states of ^{11}B were reasonably reproduced by the calculations as shown in Fig. 6.

The $3/2^-_3$ states at the excitation energy $E^* \sim 8$ MeV, ^{11}B($3/2^-_3$, 8.65 MeV) and ^{11}C($3/2^-_3$, 8.10 MeV) are experimentally known to have abnormal properties such as weak GT and $M1$ transitions compared with normal low-lying states. It is also interesting that the $3/2^-_3$ state is missing in shell-model calculations for ^{11}B. These facts suggest that $3/2^-_3$ may not be an ordinary shell-model-like state but may have a developed cluster structure. The AMD calculations for ^{11}B give good results for the energy levels including the $3/2^-_3$ state (Fig. 6) and reproduce well the experimental values of transition strengths. For the $3/2^-_3$ state, the quenchings of GT and $M1$ transitions

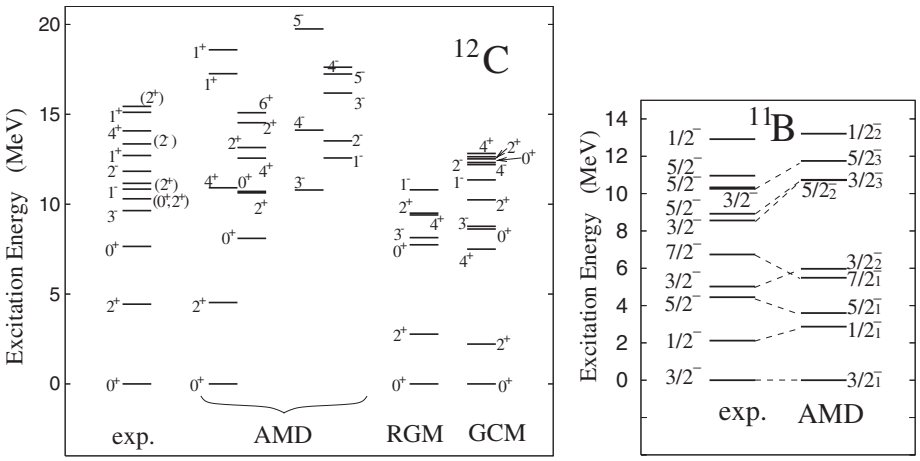

Fig. 6. Left: Energy levels of ^{12}C calculated with AMD-VAP [67]. The theoretical levels of ^{12}C calculated with the 3αRGM [71,72] and 3αGCM [73–75] are also shown. Right: Energy levels of ^{11}B calculated with AMD-VAP [68].

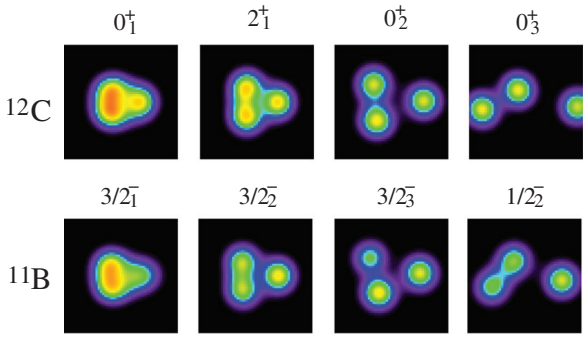

Fig. 7. Density distributions of intrinsic states for the ground and excited states of ^{12}C and ^{11}B calculated by AMD-VAP [67,68].

are understood because of the developed cluster structure of the $3/2^-_3$ state which has a small overlap with the low-lying shell-model-like states. Indeed, the $3/2^-_3$ states of ^{11}C and ^{11}B exhibit remarkably well developed 2α+^{3}He and $2\alpha + t$ clustering (Fig. 7).

3.2.3. Analogy of cluster aspects of ^{11}B to ^{12}C. Comparing the results for ^{11}B with those for ^{12}C, we found good analogies of cluster aspects between ^{11}B and ^{12}C. As shown in Fig. 7, the ground state of ^{11}B is described by a $p_{3/2}$-shell configuration with mixing of the cluster structure, as is that of ^{12}C. The development of the $2\alpha + t$-cluster core in ^{11}B$(3/2^-_2)$ shows a good analogy to that of the 3α-cluster core in ^{12}C(2^+_1). The remarkably well developed $2\alpha + t$-cluster structures in ^{11}B$(3/2^-_3)$ and ^{11}B$(1/2^-_2)$ can be associated with the developed 3α cluster in ^{12}C(0^+_2) and ^{12}C(0^+_3), respectively.

Particular attention is paid to the analogy of ^{11}B$(3/2^-_3)$ to ^{12}C(0^+_2). Similarly to the case of ^{12}C(0^+_2), the ^{11}B$(3/2^-_3)$ wave function has a large overlap with various $2\alpha + t$ configurations, indicating that the state has no geometric cluster configuration but it should be regarded as a weakly interacting $2\alpha + t$-cluster state. The root-mean-square radius (r.m.s.r.) of the ^{11}B$(3/2^-_3)$ state is 3.1 fm; this is remarkably large compared with that of the ground state (2.5 fm). Considering the amplitudes of the wave function fragmented on various configurations and the large radius, the $3/2^-_3$ state may be a $2\alpha + t$-cluster state with a dilute density like a gas, where clusters are rather freely moving. It should

be noted that, for $^{11}\mathrm{B}(3/2^-_3)$, the energy position relative to the three-cluster break-up threshold is lower and the nuclear size is smaller than those for $^{12}\mathrm{C}(0^+_2)$, and therefore the gas-like feature of $^{11}\mathrm{B}(3/2^-_3)$ might be weaker than $^{12}\mathrm{C}(0^+_2)$.

Another analogy between $^{11}\mathrm{B}(3/2^-_3)$ and $^{12}\mathrm{C}(0^+_2)$ is the remarkable monopole transition strengths from the ground state. The calculated iso-scalar monopole strength $B(IS0)$ for the transition $3/2^-_1 \to 3/2^-_3$ is 94 fm^4 and this value is in good agreement with the experimental value 94±16 fm^4[76]. The $B(IS0)$ value is as large as that for the monopole transition $0^+_1 \to 0^+_2$ in $^{12}\mathrm{C}$.

Recently, structures of $^{11}\mathrm{B}$ have also been investigated by the $2\alpha + t$ orthogonality condition model (OCM) [77]. In the $2\alpha + t$ OCM results, different cluster features between $^{11}\mathrm{B}(3/2^-_3)$ and $^{12}\mathrm{C}(0^+_2)$ have been demonstrated from the point of view of α condensation. The cluster gas features of $^{11}\mathrm{B}$ are under discussion.

3.2.4. Cluster structures of ^{14}C. As mentioned, the straight-line chain structure of three α clusters may not be stable in $^{12}\mathrm{C}$ even though the linear-chain-like 3α state with an obtuse triangle configuration might exist in the 0^+_3 state. We here consider the cluster structures of $^{14}\mathrm{C}$, in which 3α-core structures with an additional two neutrons are expected.

The structures of excited states of $^{14}\mathrm{C}$ were investigated with a method of β–γ constraint AMD in combination with GCM by Suhara and one of the authors (Y.K.-E.) [69]. We stress again that the existence of clusters was not assumed in the model but the dynamics of fourteen nucleons was solved in the AMD model space. The results suggest a variety of developed 3α-cluster core structures in excited states. One of the new findings is that a 3α linear-chain structure with valence neutrons can be stabilized in $^{14}\mathrm{C}$ and may construct a $K^\pi = 0^+$ rotational band above the $^{10}\mathrm{Be} + \alpha$ threshold energy (Fig. 8). As shown in the density distributions of protons and neutrons, the linear-chain state indicates a strongly coupling $^{10}\mathrm{Be} + \alpha$ cluster structure, where an α cluster is sitting on the head of a deformed $^{10}\mathrm{Be}$ cluster. It was found that additional neutrons play an important role in stabilizing the linear-chain configuration. Unfortunately, there is no experimental evidence for the linear-chain state. Observations of $^{10}\mathrm{Be} + \alpha$ decay [78,79] would be helpful in identifying it.

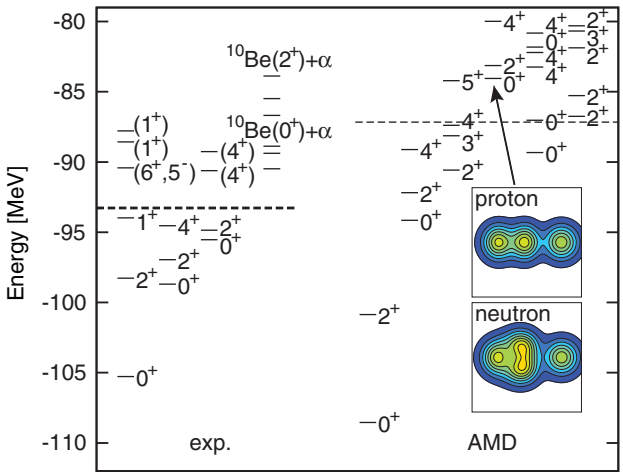

Fig. 8. Energy levels of $^{14}\mathrm{C}$. The theoretical data are those in Ref. [69] calculated with $\beta - \gamma$ constraint AMD with GCM by using the Volkov No.2 force with $B = H = 0.125$, $M = 0.60$ and the G3RS-type spin–orbit force with $u_I = -u_{II} = 1600$ MeV. Proton and neutron density distributions for the linear-chain $K^\pi = 0^+$ band are also shown. The dotted lines are the experimental and theoretical $^{10}\mathrm{Be} + \alpha$ threshold energies. The figure is taken from personal communications with T. Suhara.

3.3. Spectroscopy and exotic phenomena in the island of inversion

Neutron-rich Ne and Mg isotopes around the $N \sim 20$ region called the "island of inversion" are known to have anomalous properties [80]. These anomalies originate in the quenching of the $N = 20$ shell gap in neutron-rich nuclei, leading to the breakdown of the magic number $N = 20$ and large nuclear deformation. This drastic change of nuclear shell structure has been intensively investigated, focusing mainly on the spectral properties of yrast states [81–86]. Recently, thanks to developments in experimental techniques, information on non-yrast states [87–90] has rapidly increased to reveal exotic phenomena peculiar to the island of inversion. For example, "the coexistence of spherical and deformed shapes" and "the coexistence of normal and intruder configurations" have been discussed based on the discovery of the second excited 0^+ states of ^{30}Mg [88] and ^{32}Mg [90].

AMD combined with GCM is one of the most powerful theoretical approaches to investigate the non-yrast states of nuclei in the island of inversion as well as the yrast states [8,9,91–94]. Here we introduce some recent AMD studies for shape coexistence, one-neutron halo and molecular structure in the island of inversion.

3.3.1. Many-particle and many-hole states and shape coexistence in ^{31}Mg. The neutron orbits and the coexistence of normal and intruder configurations in neutron-rich Ne and Mg isotopes are most sensitively probed by the low-lying yrast and non-yrast states of odd-mass isotopes. The last neutron's orbit, which determines the spin and parity of the ground state, is quite sensitive to nuclear deformation.

As one of such examples, Fig. 9 shows the calculated energy surface, and predicted [93] and observed spectra of ^{31}Mg [95–102]. The energy surface of ^{31}Mg [Fig. 9(a)] has low-lying local minima with different nuclear deformations. By calculating the occupation probabilities of single-particle orbits, these local minima are found to correspond to the 0p1h, 1p2h, 2p3h, and 3p4h neutron configurations in ascending order of deformation. Here the particle–hole configurations are labeled relative to the $N = 20$ shell closure and the nuclear deformation becomes larger as the numbers of particles in the pf shell and holes in the sd shell increase. To predict the ground-state configuration, it

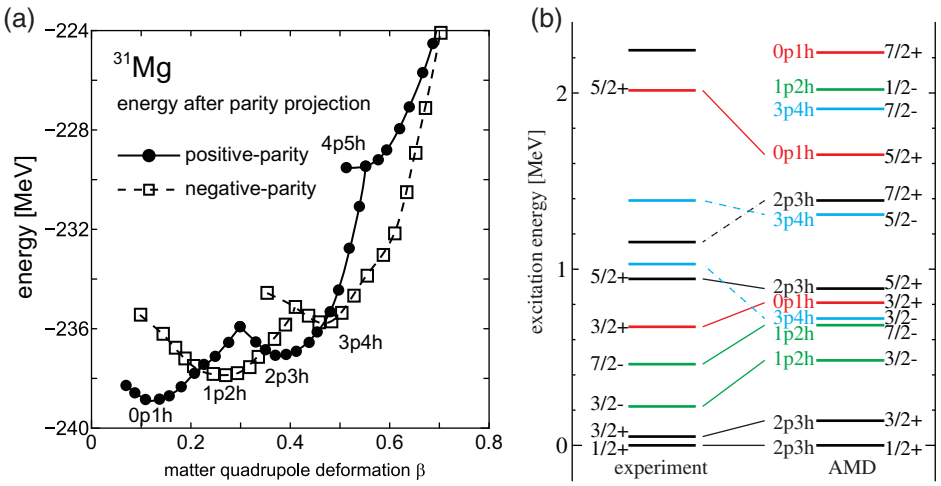

Fig. 9. (a) Energy surfaces of the positive- and negative-parity states of ^{31}Mg as a function of the quadrupole deformation parameter β calculated by AMD. The AMD results are taken from Ref. [93]. (b) Low-lying spectrum of ^{31}Mg calculated by AMD + GCM compared with the experimental assignment suggested in Ref. [95].

is essential to perform a GCM calculation. In fact, the AMD + GCM calculation [Fig. 9 (b)] shows that the ground state is strongly deformed and that an almost pure 2p3h configuration exists in which two neutrons are promoted into the pf shell across the $N = 20$ shell gap to break down the magic number. The calculated magnetic moment of the ground state is $-0.91\mu_N$, while the observed value is $-0.88\mu_N$ [96]. Since the spherical 0p1h states in which the $N = 20$ magicity is retained give a positive magnetic moment, the breakdown of the $N = 20$ magic number is confirmed without ambiguity. AMD predicts that the ground state is followed by $3/2^+_1$, $5/2^+_1$ and $7/2^+_1$ states with 2p3h configuration to constitute the rotational ground band due to the strong deformation. Furthermore, due to the quenching of the $N = 20$ shell gap, the coexistence of three different configurations at small excitation energy is also predicted. The 1p2h configuration appears as the $3/2^-_1$ and $7/2^-_1$ states at very small excitation energies, the strongly deformed 3p4h configuration constitutes the $K^\pi = 3/2^-$ rotational band starting from 720 keV, and the normal 0p1h configuration appears as the $5/2^+_2$ state at 1.6 MeV. Most of these excited states have been observed, in good agreement with AMD predictions, by measurements of β-decays [97–99], one proton or neutron knockout reactions [101,102], and Coulomb excitation [100]. Thus, the coexistence of various neutron configurations and deformed states is now established. For recent discussions on other nuclei, readers are directed to Ref. [94].

3.3.2. Neutron-halo with a deformed core in the island of inversion. As an example of one of the fascinating phenomena in the island of inversion, we focus on the one-neutron halo structure of ^{31}Ne. Recent experiments at the RI Beam Factory in RIKEN have revealed the large Coulomb breakup cross section [103] and interaction cross section [104,105] of ^{31}Ne, and the p- or s-wave neutron-halo structure has been suggested from analysis of the Coulomb breakup [103,106]. Usually, the neutron-halo structure is discussed based on the "spherical inert core + weakly bound neutron" models as has been done for ^{6}He and ^{11}Li. However, in this case, the core nucleus ^{30}Ne is located in the middle of the island of inversion and the assumption of a spherical inert core is inadequate. The last neutron of ^{31}Ne may be coupled to the strongly deformed core with a broken magic number. Therefore, an analysis based on a full microscopic theory is more suitable and necessary. Since a single-particle wave function is represented by a Gaussian wave packet, AMD cannot properly describe the tail part of the halo nucleus which shows exponential damping. This shortage is overcome by combining AMD with the resonating group method (AMD + RGM). We use the RGM-type wave function for ^{31}Ne,

$$\Psi_{JM} = \sum_{\alpha l} c_{\alpha l} \mathcal{A}[\chi_{\alpha l}(r) Y_{lm}(\hat{r}) \phi_n \phi^{^{30}\mathrm{Ne}}(\alpha)]_{JM}, \tag{3.1}$$

where ϕ_n and $\chi_{\alpha l}(r)Y_{lm}(\hat{r})$ are the spin wave function of the valence neutron and the relative motion between the valence neutron and ^{30}Ne, respectively. $\phi^{^{30}\mathrm{Ne}}(\alpha)$ is the internal wave function of ^{30}Ne solved by AMD + GCM [92], and α labels the ground and excited states of ^{30}Ne. Since the AMD wave function of ^{30}Ne is a superposition of the Slater determinant of Gaussians, the coefficients $c_{\alpha l}$ and the relative wave function $\chi_{\alpha l}(r)$ can be solved by transforming Eq. (3.1) into a GCM type wave function. Recent developments in high-performance computing have enabled this CPU-demanding calculation.

Figure 10(a) shows the predicted spectrum of ^{31}Ne by AMD + RGM. The ground state is the $3/2^-$ state and the calculated one neutron separation energy is $S_n = 0.45$ MeV, while the observed value is 0.29 ± 1.64 MeV [107]. Due to this small separation energy, the density distribution of ^{31}Ne calculated by AMD + RGM shows a long tail at large distances, indicating a p-wave halo ($1p_{3/2}$-neutron coupled to ^{30}Ne) as shown in Fig. 10(b). The effect of the deformed core appears as the core excitation. From the coefficients $c_{\alpha l}$, it is found that the $p_{3/2} \otimes {}^{30}\mathrm{Ne}(2^+)$ configuration amounts to

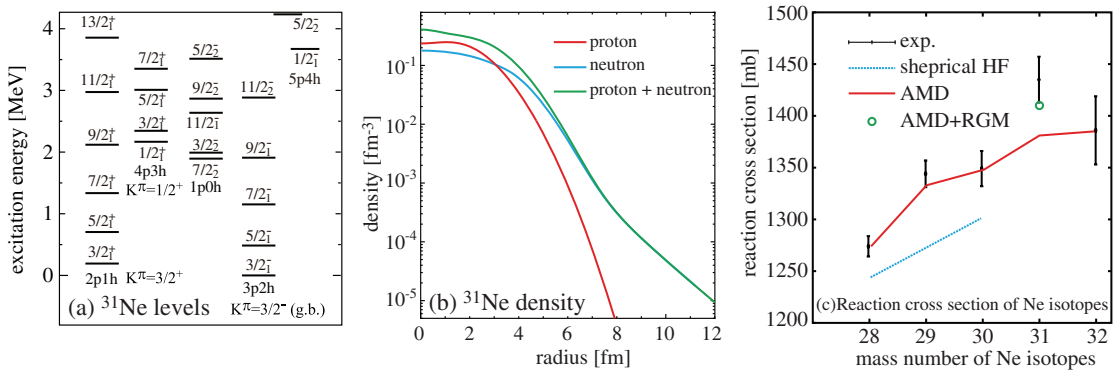

Fig. 10. (a) Low-lying spectrum of ^{31}Ne calculated by AMD + RGM. The dashed line shows the one neutron threshold energy. (b) Proton, neutron, and proton + neutron densities of the ^{31}Ne ground state ($J^\pi = 3/2^-_1$) calculated by AMD + RGM. (c) Reaction cross section of Ne isotopes calculated by the double-folding model using the density distribution obtained by AMD (solid line), AMD + RGM (open circle for ^{31}Ne) compared with the observed data [104,105]. The results are taken from Refs. [94,108].

41%, which is larger than the $p_{3/2} \otimes {}^{30}\mathrm{Ne}(0^+)$ configuration which amounts to 37%. These values suggest that the $p_{3/2}$ neutron is coupled to the deformed and rotating ground band of ^{30}Ne. Using AMD and AMD + RGM wave functions, the reaction cross sections of ^{31}Ne and other Ne isotopes are analyzed based on the double-folding model [108,109]. Figure 10(c) compares the calculated and observed reaction cross sections. We can see that the AMD wave function shows overall agreement with the observation except for ^{31}Ne, and anomalously large cross section of ^{31}Ne is reasonably described by employing the AMD + RGM wave function. Thus, with the help of high-performance computing, AMD combined with RGM and reaction theory is a promising method to investigate neutron-halo nuclei and their reactions in the heavier mass region. We can find many other candidates for the weakly bound system such as ^{35}Mg and ^{37}Mg from the systematics of the binding energy, and analysis of them is now ongoing.

3.3.3. Molecule-like states in the island of inversion. Another example of exotic phenomena in the island of inversion is the molecule-like structure in the highly excited region. As discussed in Subsection 3.1, several excited states of O, F and Ne isotopes have been predicted to have a molecule-like structure analogous to Be isotopes [46,110]. In particular, candidates for molecule-like states have recently been observed in $^{18\sim20}$O [111–113] and found to qualitatively agree with the AMD predictions [110]. Thus the exploration of molecule-like structure is expanding to heavier neutron-rich systems. In the case of F and Ne isotopes, since the neutron drip line is farther extended than for O isotopes, we can expect a molecule-like structure with more valence neutrons and more exotic phenomena.

Figure 11 shows the energies of the F isotopes obtained by AMD + GCM [50] as an example. All of these F isotopes have molecule-like states in their excited states and there are always two kinds of molecular bands (green and blue lines in the left-hand panel of Fig. 11). In these states, one or two valence neutrons are excited into the σ orbital (pf shell) together with proton excitation from the p to the sd shell, and the α + N cluster structure develops (right-hand panel of Fig. 11). It is notable that the drastic reduction in their excitation energies toward the neutron drip line is predicted. To understand this reduction, readers are reminded of the following points. (1) As mentioned in Section 3.1, the σ orbital originates in the pf shell, and its energy is lowered in the island of inversion due to the

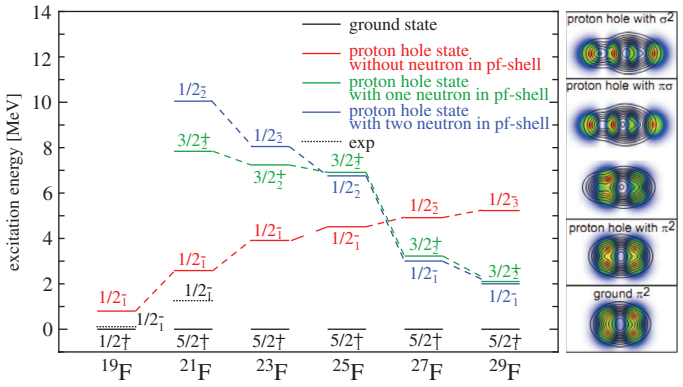

Fig. 11. Left: Band-head energies of proton hole states of F isotopes. Red lines show the states with proton excitation from the p to the sd shell and no neutron in the pf shell, while green (blue) lines show those with one (two) neutron(s) in the pf shell that have a molecule-like structure. Right: Density distribution of the core (^{19}F, contour lines) and two valence neutrons (color plot) of ^{21}F. From top to bottom, each panel corresponds to the states with two, one, and no neutrons in the pf shell with a proton hole and the ground state, respectively. This figure is reproduced from Ref. [50].

quenching of the $N = 20$ shell gap. (2) If the core has cluster structure, it induces deformation of the system and further lowers the energy of the σ orbital as in the case of Be isotopes. Therefore, the neutron excitation into the σ orbital and α clustering of the core work in a cooperative way to reduce the excitation energies of molecular states in the island of inversion. So far, several candidates for molecular states in lighter F isotopes are experimentally known [114–116]. More data for F isotopes near the drip line will be experimentally available in the near future.

3.4. Superdeformation in sd-shell nuclei

A recent development in high-spin physics is the discovery of the superdeformed band in the very small mass region ($A \sim 40$) such as ^{36}Ar [117], ^{40}Ca [118], and ^{44}Ti [119]. In contrast with heavier nuclei, these superdeformed bands are assigned from high-spin states down to very low-spin states ($J^\pi = 0^+ \sim 4^+$). From this discovery, low-lying 0^+ states that have been known for a long time are now identified as the band-head of the superdeformed bands. On the other hand, α clustering of low-lying states and molecular structure of highly excited states have long been discussed. AMD studies have been made to investigate the properties of superdeformed states and to reveal the relationship between the superdeformed states and cluster states.

3.4.1. Dual nature of superdeformed states and their evolution to molecular states. The strongly deformed excited state of ^{32}S is of particular interest for the following reasons. 1) ^{32}S ($N = Z = 16$) is a double magic nucleus of superdeformation. A couple of mean-field calculations [120–122] have predicted the superdeformed state around $E^* \sim 10$ MeV, and it has a $4\hbar\omega$ excited configuration relative to the ground state. 2) Using the unique optical potential for ^{16}O–^{16}O scattering [123,124], the ^{16}O+^{16}O cluster model [125] showed the presence of three molecular bands. Among them, the lowest energy band is located a few MeV below the ^{16}O+^{16}O threshold energy and coincides with the predicted superdeformed band mentioned above, while the highest energy band nicely reproduces the well known ^{16}O+^{16}O molecular resonances [126,127]. Thus the two different theoretical approaches give qualitatively the same result and suggest a relationship between the superdeformed states and cluster states.

AMD gives a unified understanding for the results of the mean-field and cluster model studies and shows that the superdeformed band evolves to the $^{16}O + ^{16}O$ molecular bands as the excitation energy increases [128]. Like the mean-field calculations, AMD predicts a pronounced superdeformed minimum (Fig. 12(a)). The density distribution of the superdeformed wave function clearly shows $^{16}O + ^{16}O$ molecule-like structure and the distance between $^{16}O + ^{16}O$ increases as the deformation becomes larger. Note that the superdeformed wave function is smoothly connected to the $^{16}O + ^{16}O$ cluster wave function around the Coulomb barrier ($\beta \sim 1.1$) in AMD. Around the superdeformed minimum, the ^{16}O clusters are distorted by the formation of the mean-field and by the spin–orbit interaction to gain more binding energy, while the pure $^{16}O + ^{16}O$ cluster structure is restored as the inter-cluster distance (deformation) becomes larger. The AMD + GCM calculation has shown that three rotational bands appear as the superposition of the wave functions around this superdeformed minimum (Fig. 12(b)). The lowest energy band coincides with the superdeformed band predicted by the mean-field calculations. The $^{16}O + ^{16}O$ cluster component in this band amounts to 57%, which means the superdeformed band has a $^{16}O + ^{16}O$ molecule-like structure, but the ^{16}O clusters are considerably distorted. This shows the dual nature of this band (mixing of the mean-field and cluster aspects) and explains why the mean-field calculations and cluster model give qualitatively the same results. The degree-of-freedom of inter-cluster motion embedded in the superdeformed band shows up as two excited rotational bands. The cluster components of these two bands amount to more than

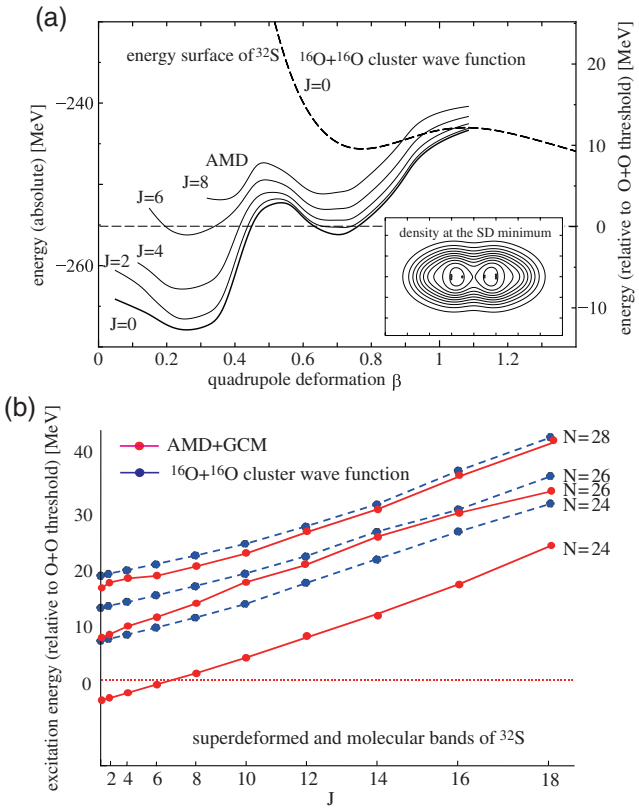

Fig. 12. (a) Energy surface of ^{32}S as a function of quadrupole deformation β. Solid lines show the energy surfaces for each angular momentum obtained by AMD, while the dashed line shows that obtained by the $^{16}O + ^{16}O$ cluster wave function. (b) Three rotational bands built around the superdeformed minimum obtained by the AMD + GCM (solid lines) and $^{16}O + ^{16}O$ cluster model wave functions. The principal quantum number N for each rotational band is also shown. The figures are reproduced from Ref. [128].

90% and these bands are interpreted as the excitation mode of the superdeformed band in which the relative motion between two ^{16}O clusters is excited by 2 and 4$\hbar\omega$, which is confirmed by analysis of the inter-cluster motion of the AMD wave function. The highest band with 4$\hbar\omega$ excitation of relative motion plausibly agrees with the observed ^{16}O +^{16}O molecular band [126,127]. Thus the superdeformed band and the molecular band can be regarded as a series of the ^{16}O +^{16}O cluster bands, and the superdeformed band evolves to the ^{16}O +^{16}O molecular band as the inter-cluster motion is excited.

3.4.2. Superdeformation and clusters in the $A \sim 40$ region. The superdeformed state and ^{16}O +^{16}O clustering of ^{32}S shed light on the relationship between the (super)deformed states and clustering. As an illustrative and interesting example, Fig. 13(a) shows the observed spectra of double magic nucleus ^{40}Ca. Two deformed rotational bands start from the 0^+ states at 3.35 and 5.21 MeV. It has been suggested that the former band is predominated by a 4$\hbar\omega$ excited configuration and the latter is an 8$\hbar\omega$ configuration [129,130]. The discovery of high-spin states [118] identified the latter band as a superdeformed band, and several theoretical studies based on the mean-field models have been performed [121,122]. On the other hand, based on the cluster model, α+^{36}Ar clustering of the band starting from 3.35 MeV has been suggested [131,132] and experimentally confirmed by the α

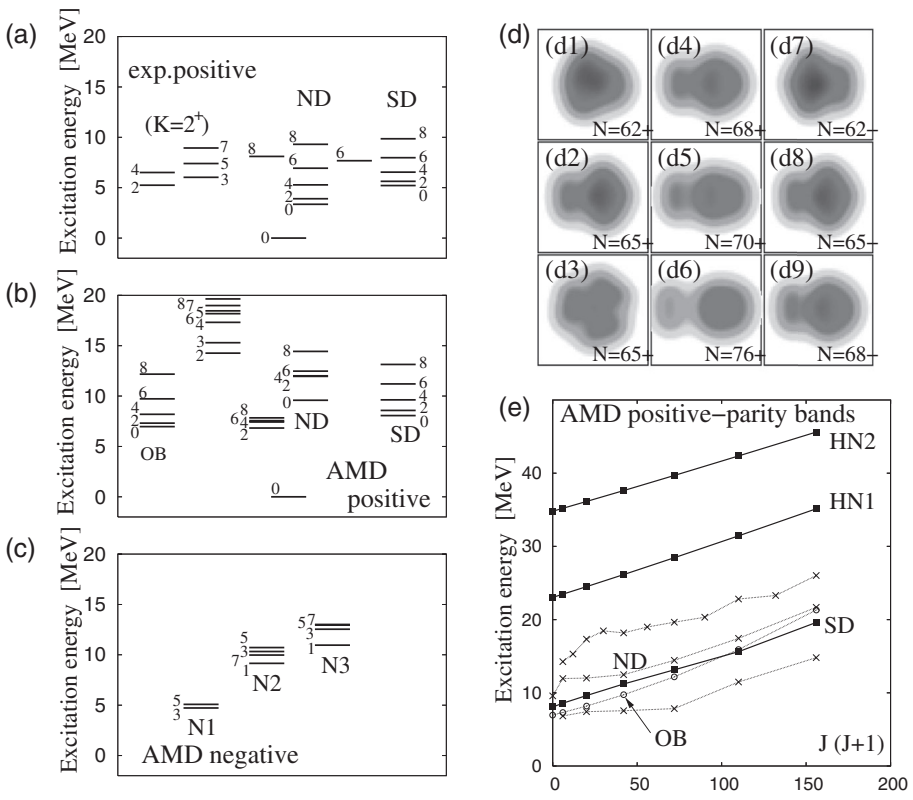

Fig. 13. (a) Observed positive-parity states of ^{40}Ca. (b) and (c) Calculated positive- and negative-parity spectra by AMD + GCM [135]. "OB", "ND", "SD", and "N3" denote the oblate and prolate deformed bands, superdeformed band, and parity doublet partner of the superdeformed band, respectively. (d1)–(d9) Intrinsic density distribution obtained by the constraint variational calculation (see text). (e) Calculated spectra of the highly excited positive-parity states. HN1 and HN2 denote the higher nodal ^{12}C +^{28}Si cluster bands in which the inter-cluster motion is excited. The figure is republished from Ref. [135].

transfer reaction on ^{36}Ar [133,134]. In the following, we denote the band starting at 3.35 MeV as the ND band and the band at 5.21 MeV as the SD band.

AMD studies have been performed to clarify the nature of the ND and SD bands [135,136] to reveal the coexistence of the different deformed bands and their relationship to the cluster structure. Here we mainly discuss the result reported in Ref. [135], in which a variational calculation is performed under the constraint of the principal quantum number of the harmonic oscillator,

$$N = \sum_{i=1}^{A} \hat{a}_i^\dagger \hat{a}_i = \sum_{i=1}^{A} \left[\frac{\mathbf{p}_i^2}{4\hbar^2 \nu} + \nu \mathbf{r}_i^2 - \frac{3}{2} \right]. \tag{3.2}$$

Here the lowest Pauli allowed value is $N = 60$, and the average number of nucleons promoted from the sd to the pf shell increases for a larger value of N. Figure 13 (d1)–(d9) show the intrinsic density distributions obtained for different values of N. For a small value of N, an almost spherical state is obtained (d1), and prolate (d2) and oblate (d3) deformed states appear with a slight increase in N. A further increase of N develops the parity asymmetric prolate deformed state (d4). The parity asymmetry of this wave function originates in the ^{12}C $+^{28}$Si cluster nature of the superdeformed state, since it evolves into a prominent ^{12}C $+^{28}$Si cluster state as N increases (d4)–(d6). An important point is that a similar ^{12}C $+^{28}$Si cluster-like state (d9) also appears in the negative-parity state with large N, while the negative-parity state with small N (d7) corresponds to the $1\hbar\omega$ excited state built on the spherical state (d1).

Several rotational bands are obtained by the superposition of these wave functions by AMD + GCM as shown in Fig. 13 (b) and (c) compared with the observed data (Fig. 13 (a)). In the positive-parity states, there are two rotational bands (denoted as ND and OB in Fig. 13 (b)) that are dominantly composed of the wave functions (d2) and (d3) respectively, predicting a prolate and oblate shape coexistence. Though the calculated excitation energy is larger than the observation, the calculated ND band is assigned to the observed band starting from 3.35 MeV from the comparison of their $B(E2)$ strengths, while the corresponding oblate deformed band has not been experimentally assigned yet.

The highlight of the result is the superdeformed band and related ones that are associated with the parity-asymmetric ^{12}C $+^{28}$Si clustering nature (Fig. 13 (d4)–(d6) and (d8)–(d9)). The calculated superdeformed band (SD in Fig. 13(b)) is dominated by the wave functions (d4)–(d6) and starts around 8 MeV, while the observed band is located at 5.21 MeV. The AMD calculation has predicted the presence of the parity doublet partner of the superdeformed band generated by parity asymmetry. The $K^\pi = 0^-$ band starting around 11 MeV in negative parity (N3 in Fig. 13 (c)) is mainly composed of the wave function shown in Fig. 13 (d9) that also demonstrates ^{12}C $+^{28}$Si clustering and can be understood as the parity doublet partner of the superdeformed band. The clustering nature of the superdeformed band also appears as two excited molecular bands that are predicted in the high excitation energy region (HN1 and HN2 in Fig. 13(e)). These bands are dominated by the wave functions with N larger than that for the superdeformed band dominated by (d4)–(d6), which indicates that they are the nodal excitation modes of the inter-cluster motion. As in the case of ^{32}S, the superdeformed band (SD) and nodal excited bands (HN1 and HN2) can be understood as a series of ^{12}C $+^{28}$Si cluster bands. Thus, observation of the parity doublet partner and nodal excited bands will be essential to reveal the clustering nature of the superdeformed band. It is also noted that the triaxial deformation of the superdeformed band has also been discussed in Ref. [136], and it has been suggested that the $K^\pi = 2^+$ band accompanies the superdeformed band.

The situation of ^{40}Ca is schematically summarized in Fig. 14. Above the ground state, a prolate and oblate shape coexistence presents as two rotational bands. The superdeformed band is also located in

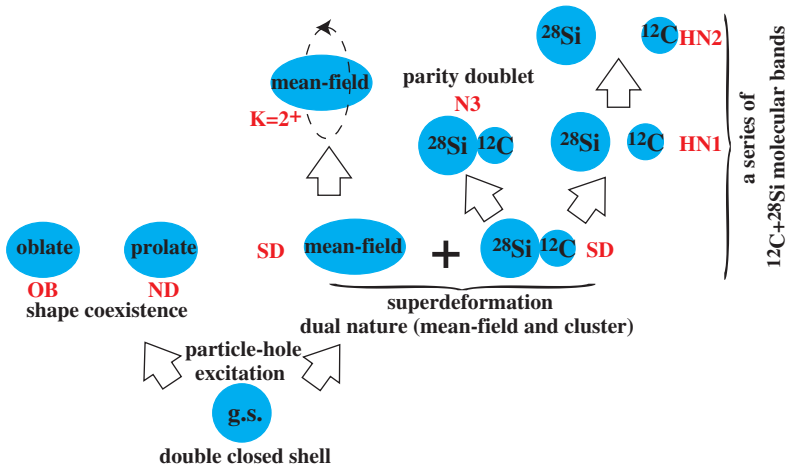

Fig. 14. Schematic figure summarizing the excitation modes of ^{40}Ca. Prolate and oblate deformed states coexist at small excitation energies. The superdeformed band has the dual nature of mean-field and ^{12}C +^{28}Si clustering. The triaxiality of the superdeformed band generates the $K^\pi = 2^+$ sideband, while parity asymmetry of the ^{12}C +^{28}Si cluster structure generates a parity doublet partner. Furthermore, the nodal excitation of the inter-cluster motion generates a series of ^{12}C +^{28}Si molecular bands.

a similar energy region and shows the dual nature of the strongly deformed mean-field and ^{12}C +^{28}Si clustering. The AMD calculation has predicted that the ^{12}C +^{28}Si clustering nature of the superdeformed band generates a parity doublet partner in the negative-parity states from parity asymmetry and the nodal excited bands in the highly excited region from excitation of the inter-cluster motion.

3.5. Decoupling between proton and neutron deformations

For $Z \neq N$ unstable nuclei, exotic phenomena concerning nuclear deformation have been discovered. If the shell effect for proton orbits and that for neutron ones compete with each other, the shape of the proton density may be affected by the neutron structure, or it might be insensitive to the neutron structure. In the latter case, decoupling of deformations between the proton and neutron densities may occur. This decoupling, i.e., different proton and neutron deformations, is possible in light-mass nuclei and it can be observed in quadrupole transition properties such as the ratio of the neutron transition matrix amplitude to the proton one (the so-called M_n/M_p ratio).

Such a decoupling between proton and neutron shapes has been suggested, for instance, in ^{16}C for which an enhanced M_n/M_p ratio called neutron dominance has been observed in the ground-band transition, $2^+_1 \to 0^+_1$, in inelastic scattering [137]. The neutron dominance was described by opposite deformations, i.e., an oblate proton shape and a prolate neutron one (Fig. 15) in the study with AMD [138,139]. Opposite deformations in ^{16}C are also supported by the abnormally small $E2$ transition strength $B(E2; 2^+_1 \to 0^+_1) = 2.6 \pm 0.9\text{e}^2\text{fm}^4$ observed by the life time measurement of the ^{16}C(2^+_1) [140]. The strength $B(E2; 2^+_1 \to 0^+_1)$ in ^{16}C is small compared with those for other C isotopes, ^{10}C, ^{12}C, and ^{14}C. The hindrance of the $B(E2; 2^+_1 \to 0^+_1)$ implies a small proton deformation; however, this seems to contradict the large deformation expected from the small excitation energy of the 2^+_1 state if proton and neutron deformations are assumed to be consistent as usual.

We studied the structure of even–even C isotopes with AMD [138,141]. The systematics of the binding energies, radii, and $E2$ transition strengths of C isotopes were qualitatively reproduced by a simple version of AMD calculations (VBP). The results indicate that the neutron shape drastically

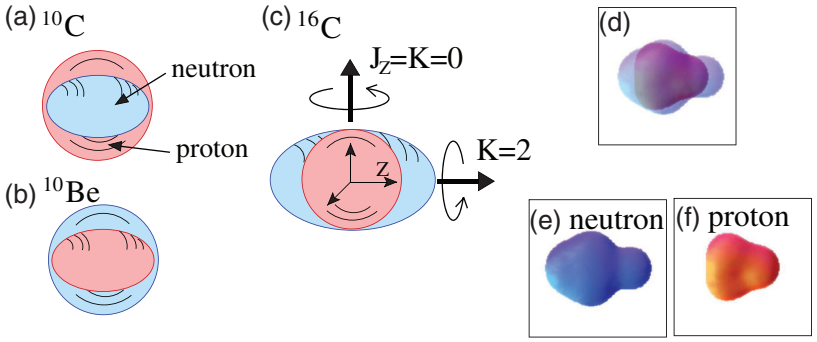

Fig. 15. Schematic figures for different shapes of proton and neutron densities in (a) ^{10}C, (b) ^{10}Be, and (c) ^{16}C. (d) Surface cut at constant proton and neutron densities of ^{16}C obtained by VBP calculations with AMD. (e) Prolate neutron density of ^{16}C. (f) Oblate proton density of ^{16}C.

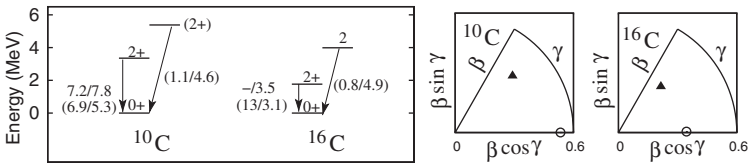

Fig. 16. Left: The experimental energy levels of the 0^+_1, 2^+_1, and 2^+_2 states and M_n/M_p ratios for $2^+_1 \to 0^+_1$ and $2^+_2 \to 0^+_1$ of ^{10}C and ^{16}C [140,142]. The experimental values for the neutron matrix amplitude (M_n) are deduced from the corresponding $B(E2)$ values of the mirror nucleus. The values in parentheses are the theoretical values for M_n/M_p from the AMD calculation [143]. Right: Deformation parameters for the intrinsic wave functions of ^{10}C and ^{16}C. The filled triangles indicate β_p and γ_p for the proton part and the open circles are β_n and γ_n for the neutron part.

changes depending on the neutron number, while the proton shape is rather stable and insensitive to the neutron structure. One of the striking features is that the difference between proton and neutron shapes is suggested in ^{16}C and ^{10}C, in which prolate neutron shapes are favored. In spite of the prolate neutron structure, the proton structure shows an oblate deformation resulting in opposite deformations. The deformation parameters for the proton and neutron densities of the intrinsic state are $(\beta_p, \gamma_p) = (0.41, 0.27\pi)$ and $(\beta_n, \gamma_n) = (0.53, 0.00\pi)$ for ^{10}C, and they are $(\beta_p, \gamma_p) = (0.32, 0.26\pi)$ and $(\beta_n, \gamma_n) = (0.34, 0.00\pi)$ for ^{16}C (Figs. 15 and 16). The reason for the opposite proton and neutron deformations is that a $Z = 6$ system favors an oblate proton shape because of the proton shell effect while an $N = 10$ or $N = 4$ nucleus shows prolate trends for the neutron shape due to the neutron shell effect. In other words, the $Z = 6$ proton structure is not so much affected by the neutron structure but keeps the oblate tendency.

To discuss the neutron deformation, mirror analysis is useful. In the mirror analysis for ^{10}C and ^{10}Be, the neutron transition matrix M_n for the ground-band transition is evaluated from $B(E2)$ in ^{10}Be by assuming mirror symmetry. The experimental value of the M_n/M_p ratio in ^{10}C deduced by the mirror analysis is described by the AMD calculation, and it can be understood with the opposite deformations between proton and neutron densities (Fig. 16). The neutron dominance in the ground-band transition is more remarkable in ^{16}C as seen in the theoretical results. Unfortunately, there are no direct data for the $E2$ strength for the mirror nuclei of ^{16}C; however, as mentioned before, the observed inelastic scattering cross section implies an enhanced M_n/M_p ratio, indicating neutron dominance [137]. It is worth mentioning that microscopic coupled-channel calculations with the

transition densities obtained by the AMD calculation have reproduced the inelastic scattering data successfully [139].

To clarify the oblate shape of the proton structure in ^{16}C and ^{10}C, observations of possible $K = 2$ side bands and their transition properties would be helpful probes. Such a nucleus with oblate proton and prolate neutron structures may show an isovector triaxiality. If this is the case, a $K = 2$ side band can be constructed from the rotation around the symmetric axis of the prolate neutron part instead of the rotation around the perpendicular axis for the $K = 0$ ground band (Fig. 15). Since the proton contribution should be dominant while the neutron contribution is minor in the rotation for the $K = 2$ side band, the inter-band transition $2^+_2 \to 0^+_1$ may show proton dominance resulting in a small M_n/M_p ratio. In fact, the calculated M_n/M_p ratios for the $2^+_2 \to 0^+_1$ in ^{10}C and ^{16}C are quenched, as shown in Fig. 16, and they indicate proton dominance. There is no experimental information on the transition strength for $2^+_2 \to 0^+_1$. Inelastic scatterings of ^{10}C and ^{16}C will be good probes to experimentally confirm the proton dominance.

4. Applications of the time-dependent AMD method to nuclear response and reaction

Interesting phenomena, including clustering phenomena, appear in nuclear many-body systems, not only near the ground state but also in excited states over a wide range of excitation energies. These include giant resonances of collective modes and stronger expansion of the system which is often followed by the disintegration into fragment nuclei. In addition to the collective degrees of freedom, the non-collective (thermal) excitations also play important roles in many cases. Since the number of states increases very rapidly as the excitation energy goes up, it is difficult to describe these phenomena based on individual quantum states. The time-dependent version of AMD has been a powerful approach for such problems of highly excited systems.

4.1. Dipole resonances

Among exotic phenomena in neutron-rich nuclei, one of the hot subjects is dipole strengths in low energy regions, which are expected to enhance in neutron-rich nuclei due to excess neutrons. For instance, soft resonances in extremely low-energy regions and pygmy resonances below giant dipole resonance (GDR) energy are attracting great interests (see, for example, Refs. [144–149] and references therein). To investigate isovector dipole responses of neutron-rich nuclei, we applied a time-dependent version of AMD without stochastic terms [150].

In order to calculate responses to external fields, we first solve the static problem and obtain the optimum parameter set Z^0, which gives the energy minimum state $\Phi_{\rm AMD}(Z^0)$ in the AMD model space. Then, we boost the $\Phi_{\rm AMD}(Z^0)$ instantaneously at $t = 0$ by imposing an external perturbative dipole field,

$$\Psi(t = 0+) = e^{-i\epsilon F}\Phi_{\rm AMD}(Z^0), \tag{4.1}$$

$$V_{\rm ext}(\mathbf{r}, t) = \epsilon F(\mathbf{r})\delta(t), \tag{4.2}$$

$$F(\mathbf{r}) = \mathcal{M}(E1, \mu) = \sum_i^A e^{\rm rec} r_i Y_{1\mu}(\hat{\mathbf{r}}_\mathbf{i}), \tag{4.3}$$

where ϵ is an arbitrary small number and $e^{\rm rec}$ is the $E1$ recoil charge, Ne/A for protons and $-Ze/A$ for neutrons. Note that the initial state $\Psi(t = 0+)$ after imposing the dipole field is written with a single AMD wave function $\Phi_{\rm AMD}(Z(t = 0+))$.

Following the time-dependent AMD method, we can calculate the time evolution of the system, $\Psi(t) = \Phi_{\rm AMD}(Z(t))$, from the initial state $\Psi(t = 0+)$ by using the equation of motion Eq. (2.5). Once the wave function $\Psi(t)$ is obtained as a function of time, the transition strength can be obtained by Fourier transform of the expectation value of $\mathcal{M}(E1, \mu)$ as follows,

$$\frac{dB(\omega; E1, \mu)}{d\omega} \equiv \sum_n |\langle n|\mathcal{M}(E1, \mu)|0\rangle|^2 \delta(\omega - \omega_n) \tag{4.4}$$

$$= -\frac{1}{\pi\epsilon}{\rm Im}\int_0^\infty dt \langle\Psi(t)|\mathcal{M}(E1, \mu)|\Psi(t)\rangle e^{i\omega t}, \tag{4.5}$$

where $|0\rangle$ is the ground state and $|n\rangle$ is the excited state with the excitation energy $\hbar\omega_n$.

In the present framework, $dB(\omega; E1)/d\omega$ consists of discrete peaks in principle, because the present AMD method is a bound state approximation and continuum states are not taken into account. We introduce a smoothing parameter Γ by hand in the Fourier transform in Eq. (4.4) which may simulate the escape and spreading widths of resonances.

One of the advantages of time-dependent AMD is that we can obtain intuitive interpretations for each mode by analyzing time evolution of Gaussian centers $\mathbf{Z}_i(t)$ of single-particle wave packets. Another advantage is that the present method is free from the spurious center-of-mass motion because center-of-mass motion can be exactly separated from $\Psi(t)$.

We applied this method to Be, B, and C isotopes and investigated the $E1$ resonances [150]. The $E1$ strengths are shown in Fig. 17. It was found that remarkable peaks appear in ^{10}Be, ^{15}B, and ^{16}C in the $E^* = 10 - 15$ MeV region decoupling from the GDR. Those soft dipole resonances arise from the relative motion of excess neutrons against a core, which is decoupled from the motion inside the core. In other words, the soft resonances appear due to the excitation of excess neutrons around the rather hard core. In fact, the strengths of the soft dipole resonances almost exhaust the cluster sum rule values for the core and valence neutrons. In further neutron-rich B and C isotopes with $N > 10$, the strengths for the soft dipole resonances decline compared with those in ^{15}B and ^{16}C. The reason for decreasing low-lying strengths is that motion of excess neutrons assimilates into neutron motion inside the core and its decoupling from the core weakens. As a result, the excitation energies of the GDR decrease with the enhancement of the neutron skin. It is striking that strengths of the soft dipole resonances do not necessarily increase with the increase of excess neutrons. Instead, the feature of the soft resonances rapidly changes depending on the proton and neutron numbers of the system. The strengths of the soft dipole resonances depends on how much the coherent motion of the excess neutrons decouples from the motion inside the core.

4.2. Radial oscillations

Radial breathing oscillations of nuclei are particularly interesting because they are closely related to the compressibility of nuclei and nuclear matter. The AMD approach is, however, not very suitable for precise analysis of the monopole strengths since the state boosted by the monopole operator from the ground-state AMD wave function is no longer an AMD state. Nevertheless, AMD can be a powerful tool to explore the radial oscillations at various amplitudes. The large amplitude oscillations should be continuously linked to the expansion of nuclei without restoration at higher energies where many-body correlations play important roles in forming clusters and fragment nuclei. Therefore, the possibility of cluster correlations in lower energy oscillations is an interesting question.

The radial oscillations of ^{12}C and other nuclei were calculated with AMD [Eq. (2.5)] without any stochastic terms in Ref. [151]. The time evolution is solved from the initial state prepared by

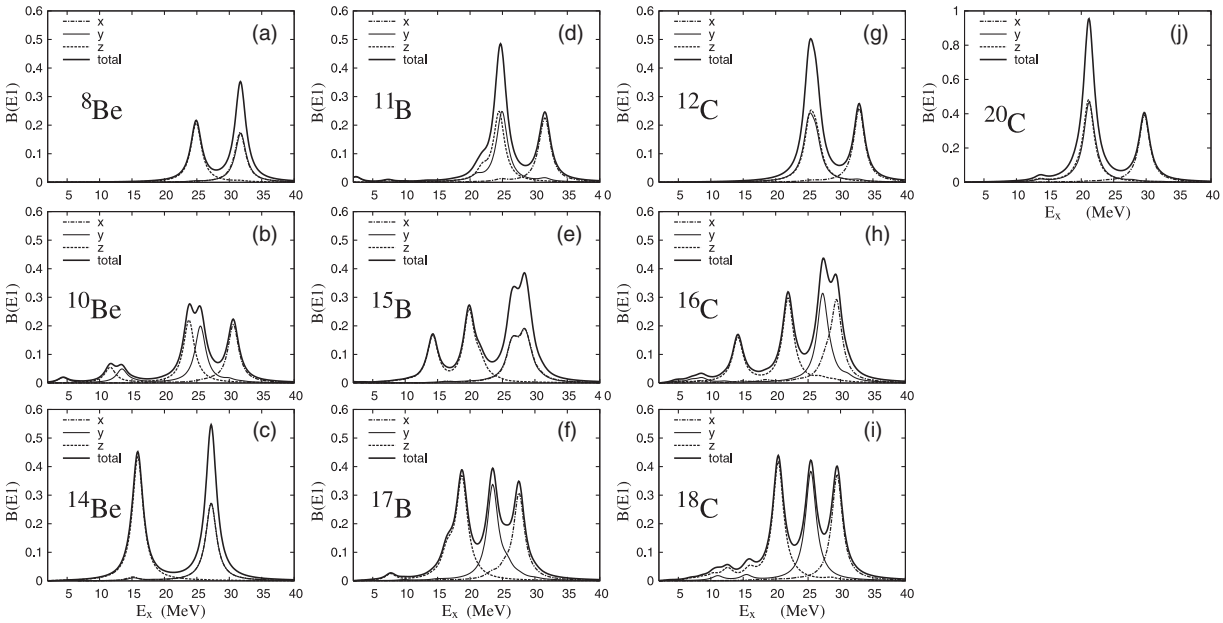

Fig. 17. $E1$ transition strengths (e^2fm^2/MeV) as functions of excitation energy of Be, B, and C isotopes calculated with the time-dependent AMD method by using the MV1 ($m = 0.576$ and $b = h = 0$) + G3RS ($u_I = -u_{II} = 900$ MeV) force. The smoothing parameter is chosen to be $\Gamma = 2$ MeV. Thin dash-dotted, solid, and dotted lines are the contribution of vibration for the x,y, and z-directions, respectively. The total strengths are shown by the thick solid lines. The figure is from Ref. [150]

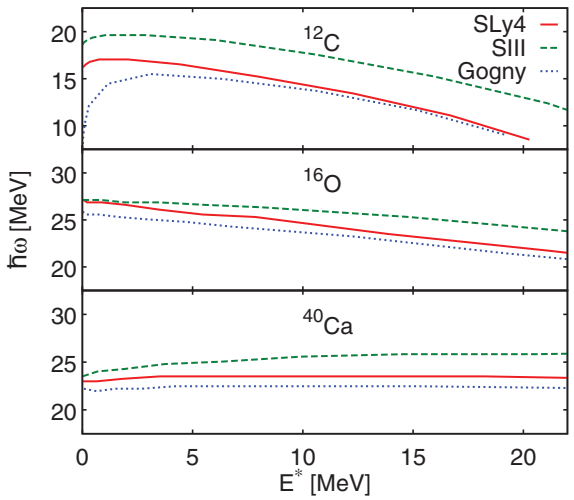

Fig. 18. AMD prediction for the frequency $\hbar\omega$ of the radial oscillation as a function of the excitation energy for ^{12}C, ^{16}O, and ^{40}Ca with the SLy4, SIII, and Gogny interactions. The nuclear matter incompressibilities for these interactions are $K = 230$, 355, and 228 MeV, respectively. The figure is reproduced from Ref. [151].

placing three α clusters on a regular triangle in the ^{12}C case. By changing the size of the initial regular triangle, oscillations with different amplitudes were studied. Figure 18 shows the dependence of the oscillation frequency on the amplitude or the excitation energy. The results for three different effective interactions are shown. The dependence on incompressibility is clearly observed. The dependence on the amplitude suggests the unharmomicity of the oscillation. It should be noted that

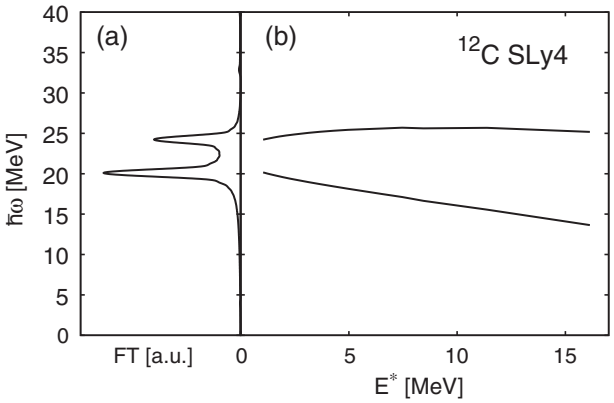

Fig. 19. (a) Fourier transform FT[r](ω) of the FMD oscillation pattern at small amplitudes, with the same initial condition as in the AMD calculation. (b) The peak position $\hbar\omega$ as a function of the oscillation amplitude. The figure is reproduced from Ref. [151].

the one-phonon excitation corresponds to the excitation energy of $E^* = \hbar\omega$ where ω is the angular frequency.

The calculations of Fig. 18 were carried out with width parameters ν that optimize the ground-state energy. Depending on the chosen width parameter, however, the frequency sometimes shows anomalous behavior as in the system of a double-well potential [151].

The same problem was studied by fermionic molecular dynamics (FMD) as well [151]. In FMD, the width parameters $\nu_i(t)$ of individual wave packets are treated as time-dependent variables as well as the centroid variables. In this case, the calculated result shows an oscillation pattern composed of two modes with different frequencies as shown in Fig. 19. By analyzing the motions of the variables, it was found that one of the two modes corresponds to a change in the wave packet widths and the other corresponds to the motion of the wave packet centroids. The latter mode is the same as that observed in the AMD result and is related to the α-clustering degrees of freedom. The former mode is the breathing of individual single-particle wave packets. Thus these calculations suggest that single-particle excitation and clustering excitation are both important in radially oscillating systems. The simplest version of AMD without any stochastic terms can describe clustering excitations.

4.3. Multifragmentation in expanding systems

It is well known experimentally that a lot of fragment nuclei are produced in each heavy-ion collision event in various situations if the incident energy is more than ten MeV/nucleon. Multifragmentation is an interesting problem in excited nuclear systems, in which quantum many-body correlations play essential roles, as well as the existence of the nuclear liquid–gas phase transition. The microscopic description of multifragmentation is, in principle, a highly complicated problem of quantum many-body systems. Transport models have been developed for heavy-ion collisions with some classical approximations. Compared with other transport models, some quantum features have been incorporated into AMD by employing fully antisymmetrized wave functions.

Figure 20 shows a typical example of the time evolution of ^{112}Sn + ^{112}Sn central collisions at 50 MeV/nucleon [152,153]. The calculation by AMD in the upper row is compared with the calculation by the stochastic mean-field (SMF) model in the lower row. In both cases, the system compressed at an early stage starts to expand almost spherically. As the expansion proceeds, a density fluctuation develops to form many fragments.

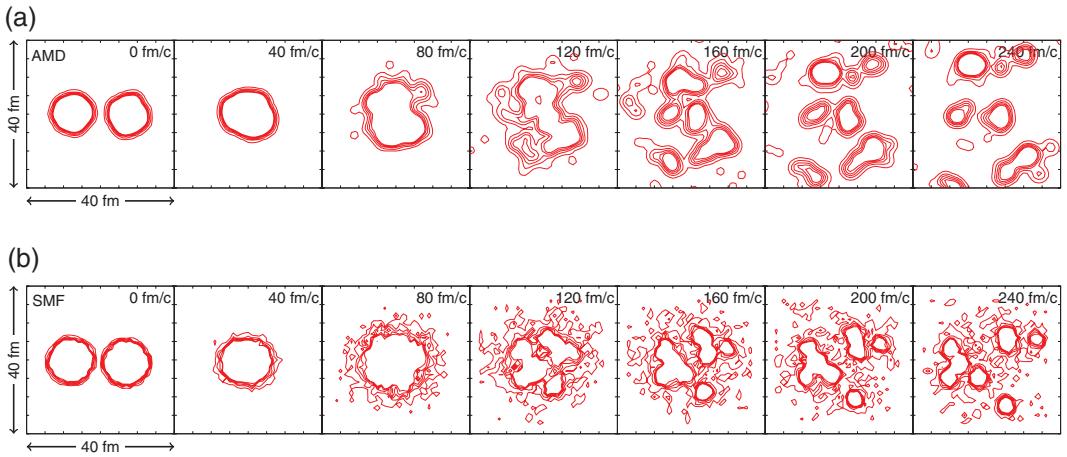

Fig. 20. Time evolution of density profiles obtained by the AMD (upper) and SMF (lower) models, for the central collision of ^{112}Sn + ^{112}Sn at 50 MeV/nucleon.

The AMD calculation was performed with the coherence time $\tau = \tau_{\rm NN}$. The SMF model, which is based on single-particle motion in the mean field, takes into account two-nucleon collisions and fluctuations [154]. Therefore these two models are conceptually similar, but the results can be different due to the different approximate treatments of fluctuations. In fact, it is observed that the density fluctuation (among different events) is already developing in AMD at the relatively early stage of $50 \lesssim t \lesssim 100$ fm/c, while the fluctuation develops in SMF only at a later stage $t \sim 100$ fm/c suggesting a fragmentation mechanism by spinodal decomposition [155]. Thus the many-body correlations are stronger in AMD. This difference can be interpreted as the origin of the differences in the expansion velocity, the nucleon emission and so on predicted by these models [152,153].

The final results of these models for the fragment charge distribution have been compared with the experimental data with reasonable success [32,156]. Figure 21 shows the AMD results compared with the data. The result depends very much on the choice of the coherence time. In this reaction system, the fragment yields for $Z \gtrsim 3$ are well reproduced by AMD when wave packet splitting with the coherence time $\tau = \tau_{\rm NN}$ is introduced. It is often convenient to define the liquid and gas parts of the system as the parts composed of $Z \geq 3$ fragments and $Z \leq 2$ particles, respectively. The comparison shows that the total charge of the liquid part, $Z_{\rm liq}$, in the AMD result (with $\tau = \tau_{\rm NN}$) is consistent with the experimental data, and therefore the total charge of the gas part, $Z_{\rm gas} = Z_{\rm system} - Z_{\rm liq}$, is also consistent.

However, a problem is found in the composition of the gas part in the result with $\tau = \tau_{\rm NN}$. The α-particle multiplicity $M_\alpha \approx 7$ is too small and the proton multiplicity $M_{\rm p} \approx 20$ is too large compared with the experimental data $M_\alpha \approx M_{\rm p} \approx 10$. It should be noted that only about 10% of the total protons in the system is emitted as free protons in this reaction at 50 MeV/nucleon. It is also known experimentally that half of the protons are still bound in clusters even at 1 GeV/nucleon [157]. Thus the experimental data suggest the importance of cluster correlations. The comparison with the data indicates that the AMD approach with wave packet splitting, which is largely based on single-particle motion in the mean field, does not include sufficient cluster correlations in the dynamics. The problem of gas composition may influence the liquid part of the system because the energy balance and the number of effective degrees of freedom will change as the gas composition changes. Therefore proper treatment of cluster correlations in dynamical approaches is an urgent issue.

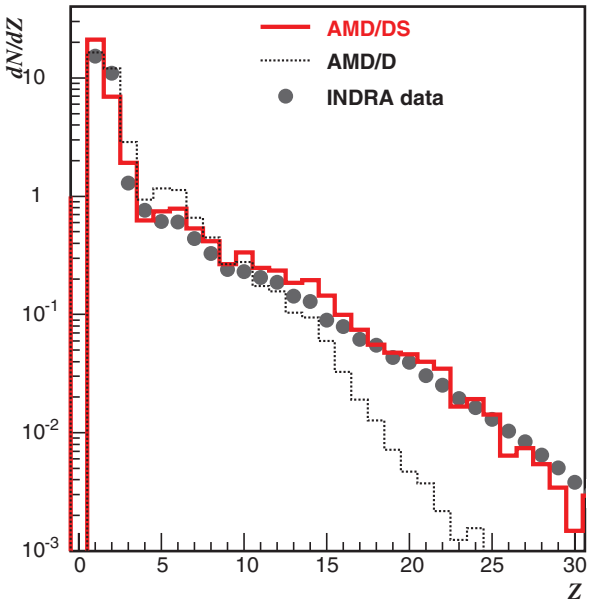

Fig. 21. The charge distribution of the clusters produced in ^{129}Xe + Sn collisions at 50 MeV/nucleon with the impact parameter $0 < b < 4$ fm, after calculating the secondary decay of excited clusters and applying the experimental filter for the detector setup. The solid histogram (labeled AMD/DS) shows the result of AMD with the coherence time $\tau = \tau_{NN}$, while the dotted histogram (labeled AMD/D) shows the result with the strongest decoherence $\tau \to 0$. The INDRA experimental data are shown by solid points. The figure is reproduced from Ref. [32].

4.4. Fragmentation in collisions of light nuclei

In an early study with AMD, fragmentation in the ^{12}C + ^{12}C reaction was studied at 28.7 MeV/nucleon [1,2]. The fragment isotope distribution is reproduced well by AMD, as shown in Fig. 22. In particular, the large production cross section of α particles is well reproduced in this case. The calculation was done with stochastic two-nucleon collisions but without wave packet splitting. Thus the situation here is different from multifragmentation in heavier systems, as seen in the previous subsection, where wave packet splitting is very important.

The detailed mechanism of the fragmentation of the ^{12}C projectile was studied in Refs. [158,159] by Takemoto *et al*. The solid line of the lower part of Fig. 23 shows the distribution of the excitation energy of the ^{12}C projectile after interaction with the target in the ^{12}C + ^{14}N reaction at 35 MeV/nucleon. In addition to the big bump around $E^* \sim 30$ MeV, there is a sharp peak at $E^* \sim 10$ MeV. The α-clustering states of ^{12}C in this energy region are strongly excited by the heavy-ion reaction, and they contribute to the large yield of α particles. In fact, the dashed line shows the contribution from the events where ^{12}C broke up into three α particles. On the other hand, in the proton-induced reactions, the excitation of ^{12}C is mainly of a single-particle nature and the α clustering states are not excited at all, as shown in Ref. [159].

For multifragmentation in ^{40}Ca + ^{40}Ca collisions at 35 MeV/nucleon, wave packet splitting plays an important role in enabling the breakup of the system into small pieces. Figure 24 compares the results without wave packet splitting and with wave packet splitting in the limit of the small coherence time $\tau \to 0$ (i.e., the strongest decoherence). The latter result is consistent with the experimental data. Without wave packet splitting, the two nuclei go through each other without forming fragments of intermediate size. Wave packet splitting allows the mixing of the two nuclei or neck formation, so

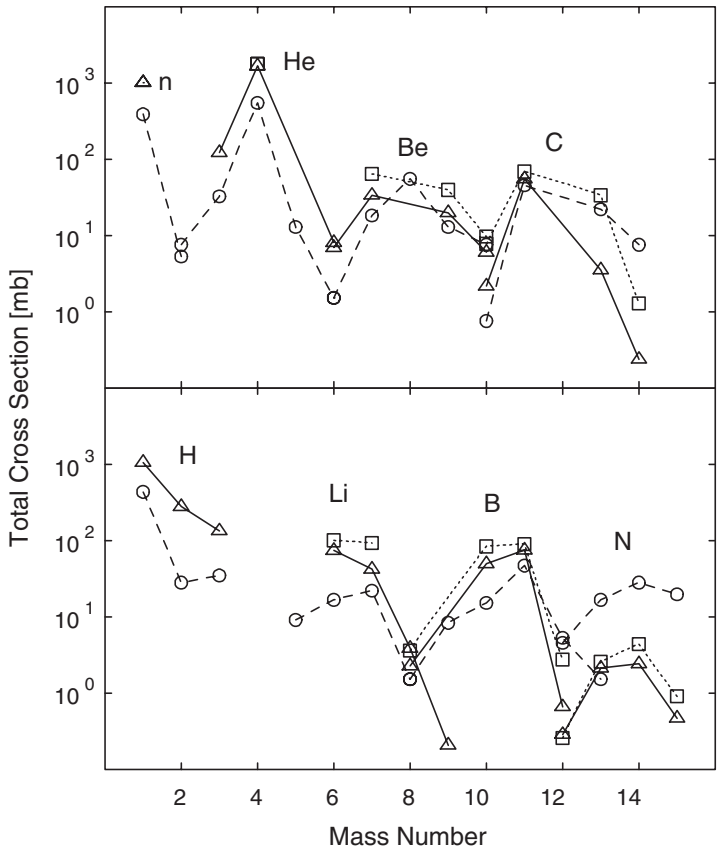

Fig. 22. Isotope distribution in $^{12}C + ^{12}C$ reaction at 28.7 MeV/nucleon. Circles are the yields before secondary decay, while triangles are those after secondary decay. Squares are the experimental data. Lines connect isotopes. The figure is reproduced from Ref. [1].

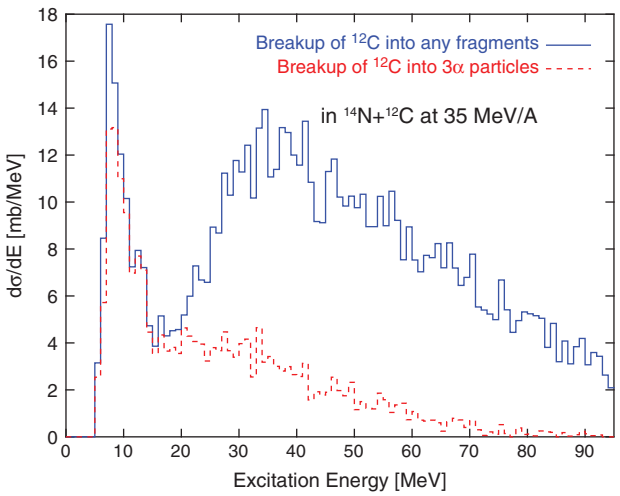

Fig. 23. The excitation energy distribution of the ^{12}C nucleus after the interaction with the ^{14}N nucleus in collisions at 35 MeV/nucleon. The figure is reproduced from Ref. [159].

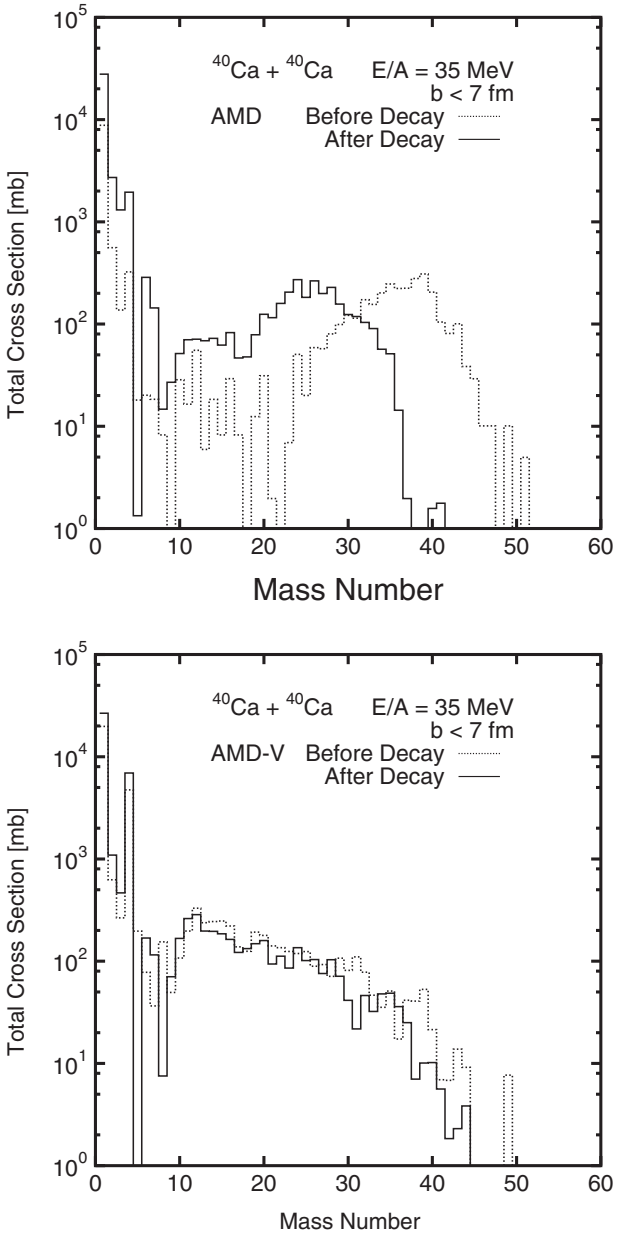

Fig. 24. Mass distribution in the ^{40}Ca + ^{40}Ca collision at 35 MeV/nucleon. Calculated results of AMD before and after the secondary decay are shown by dotted and solid histograms, respectively. The left figure is the result by AMD without wave packet splitting, and the right figure is the result with the strongest decoherence $\tau \to 0$. The figure is reproduced from Ref. [31].

that more than two fragments can be formed from the system expanding in the beam direction. The α-particle multiplicity also depends very much on wave packet splitting.

In short, the strength of the wave packet splitting (viewed from AMD) or the decoherence of the single-particle states (viewed from mean-field theory) is a key ingredient for the description of fragmentation. For stronger splitting, the system tends to expand strongly and to break into small fragments and many α particles. Unfortunately, the appropriate strength seems to depend on the size of the system and/or the incident energy. A more consistent understanding may be possible if the cluster correlations in dynamical systems are more explicitly treated.

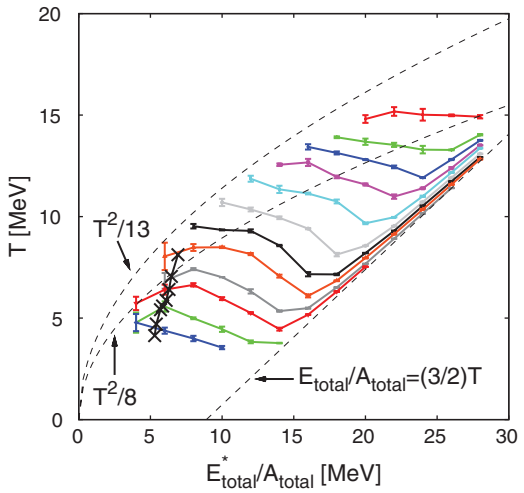

Fig. 25. Constant pressure caloric curves calculated with AMD for the $A = 36$ system. The cross symbols indicate the equilibrium state corresponding to the reaction system from $t = 80$ to 300 fm/c for ^{40}Ca + ^{40}Ca central collisions. The figure is reproduced from Ref. [169].

4.5. Statistical properties of excited systems

One of the aims of the study of multifragmentation was to extract information on excited nuclear matter in which the liquid–gas phase transition is expected, as in the system of the van der Waals equation of state. The concept of phase transition in finite many-body systems, as in heavy-ion collision systems, has been very much improved by recent studies [160,161]. Phase transition is clearly defined in finite systems by considering microcanonical ensembles.

By solving the time evolution of a many-body system in a container of a finite volume for a very long time, it is possible in principle to generate a microcanonical ensemble for the given energy and volume. However, it is a non-trivial question whether dynamical models such as AMD can produce a correct statistical ensemble. In fact, the introduction of wave packet splitting into AMD was first motivated by the need to obtain the proper statistical properties with the fermionic caloric curve $E^* = aT^2$ at low temperature [162,163]. From a different point of view, Ohnishi and Randrup also introduced stochastic terms into molecular dynamics for quantum statistics [164]. The caloric curves in the liquid–gas phase transition region were calculated by Sugawa and Horiuchi by employing AMD with an implementation of wave packet splitting [165,167]. Fermionic molecular dynamics was also applied to the caloric curves [166]. The caloric curves obtained in these studies were drawn under the condition of fixed volumes or for a system under a confining potential.

More recently, in Refs. [168,169], Furuta and Ono performed an AMD calculation to obtain constant-pressure caloric curves in which the phase transition should be clearly identified. Wave packet splitting was considered with a density-dependent coherence time $\tau(\rho)$ in this study. For a calculated microcanonical ensemble of a given energy E and a volume V, the temperature T is defined by using the kinetic energies of gas-like nucleons. The pressure P is obtained from the information of the reflections of particles at the boundary of the container. Then caloric curves are drawn as $T(E)$ for different values of P. The result for the system of $N = 18$ and $Z = 18$ is shown in Fig. 25. The nuclear liquid–gas phase transition, as a first-order phase transition, is clearly seen in this result as the back-bending of caloric curves.

The construction of microcanonical ensembles can also be regarded as a way to explore the many-body states at various excitation energies, as illustrated in Fig. 26. Above the ground state and

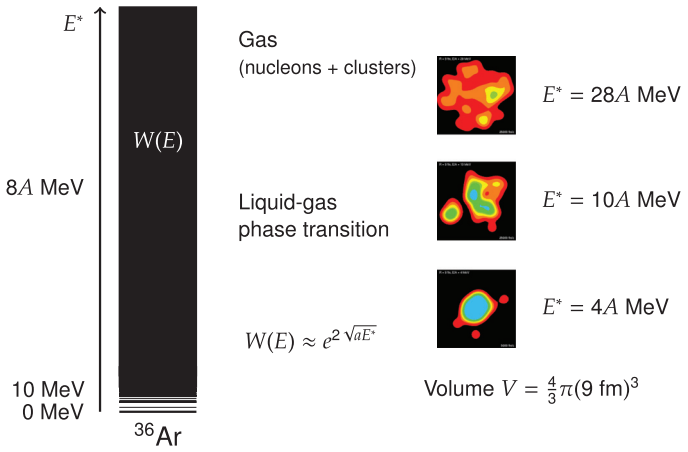

Fig. 26. Excited states of a many-nucleon system with $N = Z = 18$ confined in a virtual spherical container with a radius of 9 fm. The density distribution at each excitation energy ($E^*/A = 4$, 10, and 28 MeV) shows a snapshot taken from the AMD equilibrium calculation of Ref. [168].

low-lying excited states of the nucleus, there should be quite a lot of states which are characterized by the density of states $W(E)$. The density profile at each of the excitation energies $E^*/A = 4$, 10, and 28 MeV is a sample taken from the calculated microcanonical ensemble [168]. At low excitation energies, a single large nucleus is usually observed. The energy $E^*/A = 10$ MeV is in the liquid–gas phase transition region where $W(E)$ shows anomalous behavior and each density profile typically shows several nuclei being related to multifragmentation. It should be noted that the system confined in a container does not become a gas of nucleons even though the excitation energy is higher than the binding energy of the nucleus. When the energy is further raised to 28 MeV/nucleon, for example, the state may be regarded as a gas state but the gas is composed of clusters as well as nucleons.

Thus it is now a great advantage of AMD that it can describe both dynamical reactions in heavy-ion collisions and virtually equilibrated systems reasonably well. In Ref. [169], we investigated the question of whether equilibrium is really relevant in multifragmentation by comparing the details of reaction calculations and equilibrium calculations performed by the same AMD model. The calculations show that there exists an equilibrium ensemble which well reproduces the reaction ensemble at each reaction time t for the investigated period $80 \leq t \leq 300\,\text{fm}/c$ in $^{40}\text{Ca} + ^{40}\text{Ca}$ central collisions at 35 MeV/nucleon, as far as fragment observables (fragment yields and excitation energies) are concerned. Thus the corresponding temperature and excitation energy (or the volume and pressure) can be identified at each reaction time. In Fig. 25, the path of the reaction from $t = 80$ to $300\,\text{fm}/c$ is drawn by the cross symbols on the caloric curve figure. It is also important to note that there are some other observables which show discrepancies between the reaction and equilibrium ensembles [169]. These may be interpreted as dynamical effects in the reaction. In particular, the usual static equilibrium at each instant is not realized since any equilibrium ensemble with the same volume as that of the reaction system cannot reproduce the fragment observables.

4.6. Symmetry energy effects in heavy-ion collisions

The AMD simulations for heavy-ion collisions are useful not only to explain the experimental data but also to know what kind of information is reflected in the fragment formation. In particular, as demonstrated in the previous subsection, we may expect that statistical properties such as the equation of state can be extracted from the fragment observables even in dynamical collisions.

In heavy-ion collisions with unbalanced neutron and proton numbers, the difference between the neutron and proton motions is an interesting new degree of freedom. The difference of flow pattern between neutrons and protons has been predicted to be sensitive to the density dependence of symmetry energy. From the liquid–gas phase transition viewpoint, neutron-rich systems are quite interesting because new characters as two-component systems are expected. Namely, the gas part of the system is more neutron-rich than the liquid part; this can be called fractionation or distillation. This effect of isospin fractionation/distillation should be observable in the neutron-to-proton ratio of produced fragments.

In Refs. [171,172], the fragment yields were analyzed in the AMD simulations for multifragmentation reactions of the central collisions of Ca isotopes at 35 MeV/nucleon, in order to see how the fragment isospin composition is related to the symmetry energy term of the effective interaction adopted in the calculation. For the fragment yields $Y_i(N, Z)$ in the reaction i at $t = 300\,\mathrm{fm}/c$, it was found that the isoscaling relation

$$Y_j(N, Z)/Y_i(N, Z) \propto e^{\alpha_{ij}N+\beta_{ij}Z} \tag{4.6}$$

is satisfied for any two reaction systems i and j which differ in their proton-to-neutron ratios. Isoscaling is expected under an equilibrium assumption and has been observed in the experimental data [170]. Isoscaling is equivalent to the statement that the fragment yields are expressed as

$$Y_i(N, Z) = \exp[-K(N, Z) + \alpha_i N + \beta_i Z + \gamma_i] \tag{4.7}$$

by using a function $K(N, Z)$ that is independent of the reaction system i. If the equilibrium is relevant to the reaction, $K(N, Z)$ should contain a term $(C_{\mathrm{sym}}/T)(N - Z)^2/(N + Z)$, where C_{sym} is a kind of symmetry energy which may depend on A or Z in principle. Based on this assumption, the isoscaling parameter is related to the symmetry energy by

$$\alpha_{ij} = \frac{4C_{\mathrm{sym}}}{T}[(Z/\bar{A}_i(Z))^2 - (Z/\bar{A}_j(Z))^2], \tag{4.8}$$

where $Z/\bar{A}_i(Z)$ represents the mean isospin asymmetry of the fragments for each given Z in the reaction i.

AMD calculations were carried out with the Gogny force and the Gogny-AS force, which differ in the density dependence of the symmetry energy, as shown in Fig. 27. The result shows that the isoscaling parameter α actually depends on the density dependence of the symmetry energy as shown in Fig. 28 [171]. Furthermore, the value of C_{sym}/T extracted from the simulation result is found to be almost independent of the fragment size A or Z [172], which suggests that bulk properties are reflected in the fragment isotope yields rather than the symmetry energy for the ground-state binding energies that depends on A due to the surface effect. To explain the obtained result, C_{sym} is identified with the bulk symmetry energy at about $\frac{1}{2}\rho_0$, with ρ_0 being the saturation density of nuclear matter, and the temperature should be $T \approx 3.4$ MeV. These values for the density and the temperature are reasonable as the condition for fragmentation.

It should be noted that the above analysis has been done for fragment yields at $t = 300\,\mathrm{fm}/c$. In order to compare the results with experimental data, the effects of the decay of these primary fragments should be carefully considered.

5. Summary and perspective

In nuclear systems, cluster aspect is one of the essential features, as is mean-field aspect. The coexistence of cluster and mean-field aspects brings a variety of phenomena as functions of excitation

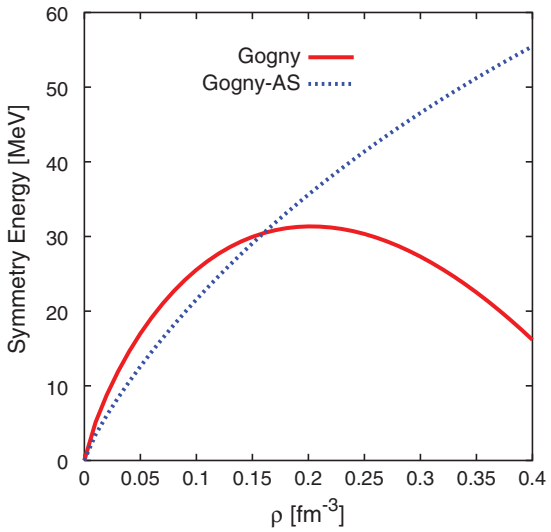

Fig. 27. Density dependence of the symmetry energy of nuclear matter for the Gogny force (solid line) and for the Gogny-AS force (dashed line).

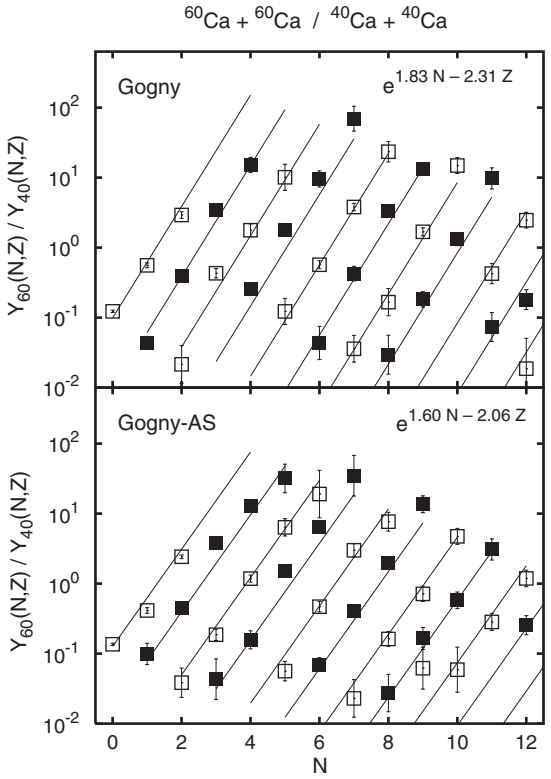

Fig. 28. The fragment yield ratio between the AMD simulations of central ^{60}Ca + ^{60}Ca and ^{40}Ca + ^{40}Ca collisions at 35 MeV/nucleon, at time $t = 300$ fm/c. The top and bottom panels show, respectively, the results obtained using the Gogny and Gogny-AS forces. The extracted isoscaling parameters are $\alpha = 1.82 \pm 0.06$ and $\beta = -2.23 \pm 0.08$ for the Gogny force, and $\alpha = 1.64 \pm 0.05$ and $\beta = -2.09 \pm 0.07$ for the Gogny-AS force. The figure is reproduced from Ref. [171].

energy and isospin degrees of freedom. With the usual theoretical models, it is not easy to describe the behaviors of both independent single nucleons in a mean field and spatially correlating nucleons in clusters. The AMD method is one of the theoretical approaches that can describe these two

aspects. In AMD, single-particle wave functions are written by localized Gaussian wave packets whose dynamics expresses the assembling and disassembling of nucleons. The method has been applied to investigate nuclear reactions and structures and it has been proved to successfully describe a variety of phenomena in general nuclei.

In this paper, we reviewed the AMD approach and its application to nuclear structure and reaction studies. To show the applicability of AMD some topics studied with time-independent and time-dependent versions of AMD were explained. In the applications of time-independent AMD to nuclear structure studies, structures of neutron-rich nuclei such as Be, C, F, Ne, and Mg isotopes were described, focusing on cluster aspects. The results suggested that a variety of structures appear in unstable nuclei as well as in stable nuclei. Deformation and cluster phenomena in $Z \sim N$ nuclei in p- and sd-shell regions were also described. The applications of time-dependent AMD include various topics such as fragmentation in heavy-ion collisions, nuclear responses, and virtual systems in thermal equilibrium. AMD calculations have successfully described multifragmentation, which is one of the remarkable phenomena in heavy-ion collisions. Comparisons with predictions by other models and/or experimental data suggest the important balance between single-particle motions and many-body correlations in the formation of clusters and fragments in these phenomena. The AMD approach is suitable to link the reaction observables to the equilibrium properties of nuclear matter such as the liquid–gas phase transition and the equation of state of asymmetric nuclear matter.

The success of these studies using the AMD approach owes a great deal to the characteristics of the AMD model, including, for instance, the advantages listed below.

- It is able to describe cluster and mean-field aspects without assuming the existence of clusters or mean fields.
- It is applicable to both static and dynamical problems.
- It it applicable to general nuclei with given proton and neutron numbers.
- Center-of-mass motion can be precisely extracted.

In addition to the above advantages, the model can be easily extended because of the flexibility of AMD wave functions. For instance, parity and angular-momentum projections and superposition of wave functions are performed in structure calculations, and stochastic collisions are incorporated in calculations of heavy-ion collisions.

The present structure studies with the AMD method cover light-mass regions of the nuclear chart up to pf-shell nuclei. Application of the method to further heavy-mass regions and the progression of systematic studies covering wide regions of the nuclear chart is a problem for the future.

The origins of cluster formation and breaking should be clarified from the point of view of nuclear force. Unfortunately, the present AMD framework is a model calculation and it requires phenomenological effective nuclear interactions. To calculate nuclear systems based on realistic nuclear forces is one of the important issues in nuclear physics. In fact, there have been many attempts at *ab initio* calculations though practical *ab initio* calculations are still limited in very light systems. For a systematic study covering a wide mass number region, model calculations are efficient. To achieve model calculations starting from realistic nuclear forces, a major problem is how to deal with complicated many-body correlations. One promising method is the unitary correlation operator method (UCOM) [173–175] recently proposed to incorporate efficiently short-range and tensor correlations in structure models such as FMD. To understand nuclear structure from a fundamental point of view, more sophisticated versions of the AMD method would be required.

Another issue of the AMD approach is wide application to reaction phenomena. Although the AMD method has been extensively applied to violent reactions above ten MeV/nucleon, its

applications to lower-energy reaction phenomena are limited. Motivated by recent progress in experimental studies, low-energy reactions such as resonances, fusion/capture, and transfer reactions are interesting problems to be solved concerning cluster phenomena in unstable nuclei.

Acknowledgments

We would like to thank A. Doté, T. Furuta, N. Furutachi, H. Horiuchi, T. Suhara, and Y. Taniguchi, for fruitful discussions and collaborations. Parts of the numerical calculations in this work were performed by using supercomputers at RCNP in Osaka University, in the High Energy Accelerator Research Organization, and at YITP in Kyoto University. This work was supported by a Grant-in-Aid for Scientific Research from the Japan Society for the Promotion of Science (No. 21540253, No. 22540275).

References

[1] A. Ono, H. Horiuchi, T. Maruyama, and A. Ohnishi, Phys. Rev. Lett. **68**, 2898 (1992).
[2] A. Ono, H. Horiuchi, T. Maruyama, and A. Ohnishi, Prog. Theor. Phys. **87**, 1185 (1992).
[3] Y. Kanada-Enyo and H. Horiuchi, Prog. Theor. Phys. **93**, 115 (1995).
[4] Y. Kanada-Enyo, H. Horiuchi, and A. Ono, Phys. Rev. C, **52**, 628 (1995).
[5] Y. Kanada-Enyo and H. Horiuchi, Phys. Rev. C, **52**, 647 (1995).
[6] A. Ono and H. Horiuchi, Prog. Part. Nucl. Phys. **53**, 501 (2004).
[7] Y. Kanada-En'yo and H. Horiuchi, Prog. Theor. Phys. Suppl. **142**, 205 (2001).
[8] Y. Kanada-En'yo, M. Kimura, and H. Horiuchi, C. R. Physique, **4**, 497 (2003).
[9] Y. Kanada-En'yo and M. Kimura, Lecture notes in Physics, **818**, 129 (2010).
[10] A. Ono, Phys. Rev. C, **59**, 853 (1999).
[11] M. Kimura and H. Horiuchi, Nucl. Phys. A, **767**, 58 (2006).
[12] Y. Kanada-En'yo, Phys. Rev. Lett. **81**, 5291 (1998).
[13] K. Ikeda, N. Takigawa, and H. Horiuchi, Prog. Theor. Phys. Suppl., extra number, 464 (1968).
[14] H. Feldmeier, Nucl. Phys. A, **515**, 147 (1990).
[15] H. Feldmeier, K. Bieler, and J. Schnack, Nucl. Phys. A, **586**, 493 (1995).
[16] A. B. Volkov, Nucl. Phys. **74**, 33 (1965).
[17] N. Yamaguchi, T. Kasahara, S. Nagata, and Y. Akaishi, Prog. Theor. Phys. **62**, 1018 (1979).
[18] R. Tamagaki, Prog. Theor. Phys. **39**, 91 (1968).
[19] J. Decharge and D. Gogny, Phys. Rev. C, **21**, 1568 (1980).
[20] J. F. Berger, M. Girod, and D. Gogny, Comput. Phys. Commun. **63**, 365 (1991).
[21] M. Beiner, H. Flocard, Nguyen Van Giai, and P. Quentin, Nucl. Phys. A, **238**, 29 (1975).
[22] E. Chabanat, P. Bonche, P. Haensel, J. Meyer, and R. Schaeffer, Nucl. Phys. A, **635**, 231 (1998); Erratum Nucl. Phys. A, **643**, 441 (1998).
[23] T. Ando, K. Ikeda, and A. Tohsaki, Prog. Theory. Phys. **64**, 1608 (1980).
[24] N. Itagaki and S. Aoyama, Phys. Rev. C, **61**, 024303 (2000).
[25] M. Kimura and H. Horiuchi, Prog. Theor. Phys. **107**, 33 (2002).
[26] M. Kimura, Phys. Rev. C, **69**, 044319 (2004).
[27] T. Suhara and Y. Kanada-En'yo, Prog. Theor. Phys. **123**, 303 (2010).
[28] S. Aoyama, N. Itagaki, and M. Oi, Phys. Rev. C, **74**, 017307 (2006).
[29] A. Doté, Y. Kanada-En'yo, H. Horiuchi, Y. Akaishi, and K. Ikeda, Prog. Theor. Phys. **115**, 1069 (2006).
[30] N. Furutachi, M. Kimura, A. Doté, and Y. Kanada-En'yo, Prog. Theor. Phys. **122**, 865 (2009).
[31] A. Ono and H. Horiuchi, Phys. Rev. C, **53**, 2958 (1996).
[32] A. Ono, S. Hudan, A. Chbihi, and J. D. Frankland, Phys. Rev. C, **66**, 014603 (2002).
[33] M. Seya, M. Kohno, and S. Nagata, Prog. Theor. Phys. **65**, 204 (1981).
[34] W. von Oertzen, Z. Phys. A, **354**, 37 (1996).
[35] W. von Oertzen, Z. Phys. A, **357**, 355 (1997).
[36] W. von Oertzen, Nuovo Cimento, **110**, 895 (1997).
[37] W. von Oertzen, Eur. Phys. J. A, **11**, 403 (1997).
[38] N. Itagaki and S. Okabe, Phys. Rev. C, **61**, 044306 (1999).
[39] N. Itagaki, S. Okabe, and K. Ikeda, Phys. Rev. C, **62**, 034301 (2000).

[40] A. Doté, H. Horiuchi, and Y. Kanada-En'yo, Phys. Rev. C, **56**, 1844 (1997).
[41] M. Ito, K. Kato, and K. Ikeda, Phys. Lett. B, **588**, 43 (2004).
[42] W. von Oertzen, M. Freer, and Y. Kanada-En'yo, Phys. Rep. **432**, 43 (2006).
[43] P. Descouvemont and D. Baye, Phys. Lett. **B505**, 71 (2001).
[44] Y. Kanada-En'yo and H. Horiuchi, Phys. Rev. C, **68**, 014319 (2002).
[45] M. Ito, N. Itagaki, H. Sakurai, and K. Ikeda, Phys. Rev. Lett. **100**, 182502 (2008).
[46] M. Kimura, Phys. Rev. **75**, 034312 (2007).
[47] S. Okabe, Y. Abe, and H. Tanaka, Prog. Theory. Phys. **57**, 866 (1977);
[48] S. Okabe and Y. Abe, Prog. Theor. Phys. **59**, 315 (1978);
[49] S. Okabe and Y. Abe, Prog. Theory. Phys. **61**, 1049 (1979).
[50] M. Kimura and N. Furutachi, Phys. Rev. C, **83**, 044304 (2011).
[51] Y. Ogawa, K. Arai, Y. Suzuki, and K. Varga, Nucl. Phys. A, **673**, 122 (2000).
[52] K. Arai, Y. Ogawa, Y. Suzuki, and K. Varga, Prog. Theor. Phys. Suppl. **142**, 97 (2001).
[53] P. Descouvemont, Nucl. Phys. A, **699**, 463 (2002).
[54] Y. Kanada-En'yo, H. Horiuchi, and A. Doté, Phys. Rev. C, **60**, 064304 (1999).
[55] Y. Kanada-En'yo and H. Horiuchi, Phys. Rev. C, **66**, 024305 (2002).
[56] T. Suzuki and T. Otsuka, Phys. Rev. C, **56**, 847 (1997).
[57] M. Freer *et al.*, Phys. Rev. Lett. **82**, 1383 (1999).
[58] M. Freer *et al.*, Phys. Rev. C, **63**, 034301 (2001).
[59] A. Saito *et al.*, Nucl. Phys. A, **738**, 337 (2004).
[60] M. Ito and Y. Sakuragi, Phys. Rev. C, **62**, 064310 (2000).
[61] Y. Fujiwara *et al.*, Prog. Theor. Phys. Suppl. **68**, 29 (1980).
[62] A. Tohsaki, H. Horiuchi, P. Schuck, and G. Röpke, Phys. Rev. Lett. **87**, 192501 (2001).
[63] Y. Funaki, A. Tohsaki, H. Horiuchi, P. Schuck, and G. Ropke, Phys. Rev. C, **67**, 051306 (2003).
[64] G. Röpke, A. Schnell, P. Schuck, and P. Nozieres, Phys. Rev. Lett. **80**, 3177 (1998).
[65] H. Morinaga, Phys. Rev. **101**, 1956 (1956).
[66] H. Morinaga, Phys. Lett. **21**, 78 (1966).
[67] Y. Kanada-En'yo, Prog. Theor. Phys. **117**, 655 (2007).
[68] Y. Kanada-En'yo, Phys. Rev. C, **75**, 024302 (2007).
[69] T. Suhara and Y. Kanada-En'yo, Phys. Rev. C, **82**, 044301 (2010).
[70] M. Chernykh, H. Feldmeier, T. Neff, P. von Neumann-Cosel, and A. Richter, Phys. Rev. Lett. **98**, 032501 (2007).
[71] Y. Fukushima and M. Kamimura, *Proc. Int. Conf. on Nuclear Structure, Tokyo, 1977*, ed. T. Marumori, J. Phys. Soc. Jpn. **44**, 225 (1978).
[72] M. Kamimura, Nucl. Phys. A, **351**, 456 (1981).
[73] E. Uegaki, S. Okabe, Y. Abe, and H. Tanaka, Prog. Theor. Phys. **57**, 1262 (1977).
[74] E. Uegaki, Y. Abe, S. Okabe and H. Tanaka, Prog. Theor. Phys. **59**, 1031 (1978).
[75] E. Uegaki, Y. Abe, S. Okabe and H. Tanaka, Prog. Theor. Phys. **62**, 1621 (1979).
[76] T. Kawabata *et al.*, Phys. Lett. B, **646**, 6 (2007).
[77] T. Yamada and Y. Funaki, Phys. Rev. C, **82**, 064315 (2010).
[78] D. Price *et al.*, Phys. Rev. C, **75**, 014305 (2007).
[79] P. J. Haigh *et al.*, Phys. Rev. C, **78**, 014319 (2008).
[80] E. K. Warburton, J. A. Bechker, and B. A. Brown, Phys. Rev. C, **41**, 1147 (1990).
[81] C. Thibault *et al*., Phys. Rev. C, **12**, 644 (1975).
[82] G. Huber *et al*., Phys. Rev. C, **18**, 2342 (1978).
[83] T. Motobayashi *et al*., Phys. Lett. B, **346**, 9 (1995).
[84] A. Poves and J. Retamosa, Phys. Lett. B, **184**, 311 (1986).
[85] N. Fukunishi, T. Otsuka, and T. Sebe, Phys. Lett. B, **296**, 279 (1992).
[86] Y. Utsuno, T. Otsuka, T. Mizusaki, and M. Honma, Phys. Rev. C, **60**, 054315 (1999).
[87] S. Takeuchi *et al*., Phys. Rev. C, **79**, 054319 (2009).
[88] W. Schwerdtfeger *et al*., Phys. Rev. Lett. **103**, 012501 (2009).
[89] Z. M. Wang *et al*., Phys. Rev. C, **81**, 064301 (2010).
[90] K. Wimmer *et al*., Phys. Rev. Lett. **105**, 252501 (2010).
[91] M. Kimura and H. Horiuchi, Prog. Theor. Phys. **107**, 33 (2002).
[92] M. Kimura and H. Horiuchi, Prog. Theor. Phys. **111**, 841 (2004).
[93] M. Kimura, Phys. Rev. C, **75**, 0413012 (2007).

[94] M. Kimura, arXiv:1105.3281v1.
[95] G. Neyens, Phys. Rev. C, **84**, 064310 (2011).
[96] G. Neyens *et al*., Phys. Rev. Lett. **94**, 022501 (2005).
[97] G. Klotz *et al*., Phys. Rev. C, **47**, 2502 (1993).
[98] H. Mach *et al*., Eur. Phys. J. A, **25**, 105 (2005).
[99] C. M. Mattoon *et al*., Phys. Rev. C, **75**, 017302 (2007).
[100] M. Seidlitz *et al*., Phys. Lett. B, **700**, 181 (2011).
[101] J. R. Terry *et al*., Phys. Rev C, **77**, 014316 (2008).
[102] D. Miller *et al*., Phys. Rev. C, **79**, 054306 (2009).
[103] T. Nakamura *et al*., Phys. Rev. Lett. **103**, 262501 (2009).
[104] M. Takechi *et al*., Nucl. Phys. A, **834**, 412c (2010).
[105] M. Takechi *et al*., Mod. Phys. Lett. A, **25**, 1878 (2010).
[106] W. Horiuchi, Y. Suzuki, P. Capel, and D. Baye, Phys. Rev. C, **81**, 024606 (2010).
[107] B. Jurado *et al*., Phys. Lett. B, **649**, 43 (2007).
[108] K. Minomo, T. Sumi, M. Kimura, K. Ogata, Y. R. Shimizu, and M. Yahiro, Phys. Rev. C, **84**, 034602 (2011).
[109] K. Minomo, T. Sumi, M. Kimura, K. Ogata, Y. R. Shimizu, and M. Yahiro, Phys. Rev. Lett., in press.
[110] N. Furutachi, M. Kimura, A. Doté, Y. Kanada-En'yo, and S. Oryu, Prog. Theor. Phys. **119**, 403 (2008).
[111] M. Milin *et al*., Eur. Phys. J. A, **41**, 335 (2009).
[112] W. von. Oertzen *et al*., Eur. Phys. J. A, **43**, 17 (2010).
[113] W. von. Oertzen *et al*., Eur. Phys. J. A, **46**, 345 (2010).
[114] G. Th. Kaschl *et al*., Nucl. Phys. A, **155**, 417 (1970).
[115] G. Mairle *et al*., Nucl. Phys. A, **363**, 413 (1981).
[116] Z. Elekes, *et al*., Phys. Lett. B, **599**, 17 (2004).
[117] C. E. Svensson *et al*., Phys. Rev. C, **63**, 061301 (2001).
[118] E. Ideguchi *et al*., Phys. Rev. Lett. **87**, 222501 (2001).
[119] C. D. O'Leary *et al*., Phys. Rev. C, **61**, 064314 (2001).
[120] R. R. Rodriguez-Guzman, J. L. Egido, and L. M. Robledo, Phys. Rev. C, **62**, 054308 (2000).
[121] T. Inakura *et al.*, Nucl. Phys. A, **710**, 261 (2003).
[122] M. Bender, H. Flocard, and P.-H. Heenen, Phys. Rev. C, **68**, 044321 (2003).
[123] M. P. Nicoli *et al*., Phys. Rev. C, **60**, 064608 (1999).
[124] W. von Oertzen, H. G. Bohlen, and D. T. Khoa, Nucl. Phys. A, **722**, 702 (2003).
[125] S. Ohkubo and K. Yamashita, Phys. Rev. C, **66**, 021301(R) (2002).
[126] M. Gai *et al*., Phys. Rev. Lett. **47**, 1878 (1981).
[127] K. Morita *et al*., Phys. Rev. Lett. **55**, 185 (1985).
[128] M. Kimura and H. Horiuchi, Phys. Rev. C, **69**, 051304(R) (2004).
[129] W. J. Gerace and A. M. Green, Nucl. Phys. A, **93**, 110 (1967).
[130] W. J. Gerace and A. M. Green, Nucl. Phys. A, **123**, 241 (1969).
[131] T. Ogawa, Y. Suzuki, and K. Ikeda, Prog. Theor. Phys. **57**, 1072 (1977).
[132] T. Sakuda and S. Ohkubo, Phys. Rev. C, **49**, 149 (1994).
[133] T. Yamaya *et al*., Phys. Lett. B, **306**, 1 (1993).
[134] T. Yamaya *et al*., Nucl. Phys. A, **573**, 154 (1994).
[135] Y. Kanada-En'yo and M. Kimura, Phys. Rev. C, **72**, 064322 (2005).
[136] Y. Taniguchi, M. Kimura, Y. Kanada-En'yo, and H. Horiuchi, Phys. Rev. C, **76**, 044317 (2007).
[137] Z. Elekes *et al.*, Phys. Lett. B, **586**, 34 (2004).
[138] Y. Kanada-En'yo, Phys. Rev. C, **71**, 014310 (2005).
[139] M. Takashina, Y. Kanada-En'yo, and Y. Sakuragi, Phys. Rev. C, **71**, 054602 (2005).
[140] H. J. Ong *et al.*, Phys. Rev. C, **78**, 014308 (2008).
[141] Y. Kanada-En'yo and H. Horiuchi, Phys. Rev. C, **55**, 2860 (1997).
[142] D. R. Tilley *et al.*, Nucl. Phys. A, **745**, 155 (2004).
[143] Y. Kanada-En'yo, Phys. Rev. C, **84**, 024317 (2011).
[144] M. Honma and H. Sagawa Prog. Theor. Phys. **84**, 494 (1990).
[145] I. Hamamoto and H. Sagawa, Phys. Rev. C, **53**, R1492 (1996).
[146] F. Catara, E.G. Lanza, M.A. Nagarajan, and A. Vitturi, Nucl. Phys. A, **624**, 449 (1997).
[147] G. Colo and P. F. Bortignon, Nucl. Phys. A, **969**, 427 (2001).
[148] T. Nakatsukasa and K. Yabana, Phys. Rev. C, **71**, 024301 (2005).

[149] T. Inakura, T. Nakatsukasa, and K. Yabana, Phys. Rev. C, **80**, 044301 (2009).
[150] Y. Kanada-En'yo and M. Kimura, Phys. Rev. C, **72**, 064301 (2005).
[151] T. Furuta, K.H.O. Hasnaoui, F. Gulminelli, C. Leclercq, and A. Ono, Phys. Rev. C, **82**, 034307 (2010).
[152] J. Rizzo, M. Colonna, and A. Ono Phys. Rev. C, **76**, 024611 (2007).
[153] M. Colonna, A. Ono, and J. Rizzo Phys. Rev. C, **82**, 054613 (2010).
[154] M. Colonna *et al.*, Nucl. Phys. A, **642**, 449 (1998).
[155] Ph. Chomaz, M. Colonna, and J. Randrup, Phys. Rep. **389**, 263 (2004).
[156] J. D. Frankland *et al.*, Nucl. Phys. A, **689**, 940 (2001).
[157] W. Reisdorf, Prog. Theor. Phys. Suppl. **140**, 111 (2000).
[158] H. Takemoto, H. Horiuchi, A. Engel and A. Ono, Phys. Rev. C, **54**, 266 (1996).
[159] H. Takemoto, H. Horiuchi and A. Ono, Phys. Rev. C **57**, 811 (1998).
[160] D. H. E. Gross, Phys. Rep. **279**, 120 (1997).
[161] D. H. E. Gross, Phys. Chem. Chem. Phys. **4**, 863 (2002).
[162] A. Ono and H. Horiuchi, Phys. Rev. C, **53**, 845 (1996).
[163] A. Ono and H. Horiuchi, Phys. Rev. C, **53**, 2341 (1996).
[164] A. Ohnishi and J. Randrup, Nucl. Phys. A, **565**, 474 (1994).
[165] Y. Sugawa and H. Horiuchi, Phys. Rev. C, **60**, 064607 (1999).
[166] J. Schnack and H. Feldmeier, Phys. Lett. B, **409**, 6 (1997).
[167] Y. Sugawa and H. Horiuchi, Prog. Theor. Phys. **105**, 131 (2001).
[168] T. Furuta and A. Ono, Phys. Rev. C, **74**, 014612 (2006).
[169] T. Furuta and A. Ono, Phys. Rev. C, **79**, 014608 (2009).
[170] H. S. Xu *et al.*, Phys. Rev. Lett. **85**, 716 (2000).
[171] A. Ono, P. Danielewicz, W. A. Friedman, W. G. Lynch, and M. B. Tsang, Phys. Rev. C, **68**, 051601(R) (2003).
[172] A. Ono, P. Danielewicz, W. A. Friedman, W. G. Lynch, and M. B. Tsang, Phys. Rev. C, **70**, 041604(R) (2004).
[173] H. Feldmeier, T. Neff, R. Roth, and J. Schnack, Nucl. Phys. A, **632**, 61 (1998).
[174] T. Neff and H. Feldmeier, Nucl. Phys. A, **713**, 311 (2003).
[175] R. Roth, T. Neff, and H. Feldmeier, Prog. Part. Nucl. Phys. **65**, 50 (2010).